Effect of Room-Temperature Pre-rolling and Pre-cryorolling on Natural Aging and Bake Hardening Response of an Al–Mg–Si Alloy

JIANRUI XING, GANG LEI, YAFEI WANG, LAXMAN BHATTA, CHARLIE KONG, and HAILIANG YU

The auto industry makes extensive use of Al–Mg–Si alloys. This study investigated the effect of pre-cryorolling and room-temperature pre-rolling on the natural aging and bake hardening response of Al–0.92Mg–0.48Si alloy. The mechanical properties were analyzed using micro-hardness, tensile, and Erichsen cupping test. Optical microscope, transmission electron microscopy, scanning electron microscopy, X-ray diffraction, and differential scanning calorimetry were used to examine the microstructure of samples. The molecular dynamics simulation was also employed to study the dislocation evolution in samples deformed at room and cryogenic temperature. The results show that both room-temperature pre-rolling and pre-cryorolling introduced immediately after solid solution treatment can effectively inhibit the adverse effects of natural aging, and promote the precipitation of strengthening phase during paint baking, leading to an improved bake hardening response. Compared with the room-temperature pre-rolling, pre-cryorolling can further improve the bake hardening response because of higher dislocation density. The results of this study indicate that pre-cryorolling with a reduction of 15 pct is the most appropriate pre-deformation procedure for this alloy, both in terms of formability and bake hardening response.

JIANRUI XING, GANG LEI, YAFEI WANG, and HAILIANG YU are with the Light Alloys Research Institute, Central South University, Changsha 410083, P.R. China and also with the State Key Laboratory of Precision Manufacturing for Extreme Service Performance, Central South University, Changsha 410083, P.R. China. Contact e-mails: yuhailiang@csu.edu.cn; yuhailiang1980@tom.com LAXMAN BHATTA is with the Advanced Materials Processing and Analysis Lab, Oregon State University, Corvallis 97330. CHARLIE KONG is with the Electron Microscope Unit, University of New South Wales, Sydney, NSW 2052, Australia.
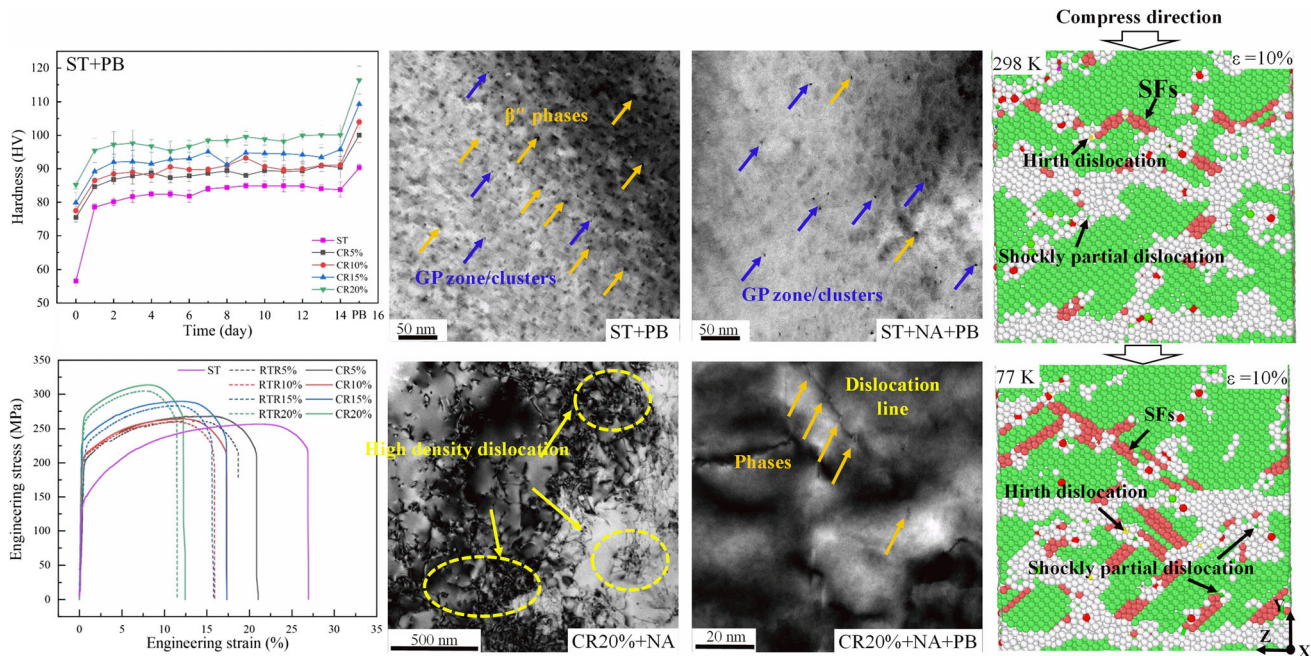
I. INTRODUCTION

THE automotive industry has extensively used Al–Mg–Si alloys as a significant lightweight material due to the alloy's low density, medium and high strength, excellent formability, and excellent welding performance.[1–3] The formation of dispersed nanoscale precipitates during aging at a high temperature can significantly improve the strength and plasticity. The precipitation sequence of Al–Mg–Si alloys is as follows: supersaturated solid solution (SSSS)—clusters—GP zone—β'' phase—β' phase—β phase (Mg$_2$Si).[4] In the process of automobile component production, this kind of high temperature aging is applied through the paint baking (PB). The bake hardening response (BHR) caused by metastable precipitated phases (mainly β'' phase) is crucial to the service performance of coatings and components.[5]

Natural aging (NA) cannot be avoided between the solid solution treatment and the forming process in Al–Mg–Si alloy plates. Due to thermodynamic instability, solute atoms within the supersaturated solid solution precipitate spontaneously at this stage, increasing initial strength and decreasing formability.[6] During the NA process, a large number of solute atoms are consumed, which hinders the precipitation of subsequent PB. Therefore, the negative effect of NA significantly reduces the BHR during paint baking, even softening the Al–Mg–Si alloys.[7] In addition, the short heat duration (20 to 30 minutes) during PB cannot give full play to the strengthening potential of the alloy, resulting in a lower yield strength compared to the peak aging state. Some researchers reported that pre-deformation could improve the BHR.[8,9]

Pre-deformation has great potential to promote the precipitation kinetics of several alloys, including Al–Mg–Si,[10] Al–Mg–Si–Cu–Zn,[11] Al–Cu–Li,[12] and Al–Mg–Cu.[13] The introduction of dislocations through pre-deformation plays an essential role in controlling precipitation mechanisms. Specifically, for Al–Mg–Si alloys, dislocations can act as sinks for vacancies, inhibiting clustering during room temperature storage and reducing the negative effect of NA.[14] Additionally, dislocations can provide heterogeneous nucleation sites for the GP zones, promoting their transformation into the β'' phase, thus improving precipitation kinetics.[15] Yin et al.[16] studied the effects of tensile pre-deformation on artificial aging hardening behavior of an Al–Mg–Si–Cu–Zn alloy. They found that 5 pct pre-tensile strain before aging significantly increased the peak aging hardness. Jia et al.[17] reported that pre-deformation of AA6022 at 443 K effectively solved the high T4 hardness caused by traditional room temperature pre-deformation treatment and provided better BHR. Dislocation and cluster (2) introduced by high-temperature pre-deformation not only inhibited the negative effect of NA, promoted β'' phase precipitation, but also reduced work hardening effect through dynamic recovery. Pre-rolling is also an important pre-deformation technique. Yuan et al.[18] investigated the effect of pre-rolling on the precipitation behavior and mechanical

properties of Al–Mg–Si–Cu–Zn alloys with different Mg/Si ratios and Cu addition amounts, and discovered that pre-rolling effectively accelerated the precipitation kinetics of the alloys. Serizawa et al.[19] found that room-temperature pre-rolling with a 5 pct reduction increased the dislocation density inside the material, and the nanoclusters along the dislocation direction preferentially transformed into β'' phase, which led to the rapid growth of β'' phase, and effectively enhanced the BHR. However, even after PB, the yield strength of these alloys is still insufficient to meet application requirements, so the BHR of these alloys is expected to be enhanced further.[20] Moreover, the primary objective of pre-deformation is to introduce dislocation in the material. There are reports that deformation at cryogenic temperature can produce high dislocation density, which has been confirmed in Al,[21] Cu,[22] Ti alloys,[23] and multilayer composites.[24] However, there have been no reports about the effect of cryogenic pre-deformation on the BHR of Al–Mg–Si alloys until now.

Currently, the majority of researches only focus on the mechanical properties of materials before and after PB[25] or disregards the influence of the NA stage.[11,18] There are few reports on the mechanical properties of materials throughout the entire solid solution treatment to bake hardening procedure. In this work, we applied pre-rolling to an Al–Mg–Si alloy with different rolling reductions (0, 5, 10, 15, 20 pct) at two temperatures

Table I. Chemical Composition of the Studied Alloy (Weight Percent)

Element	Mg	Si	Cu	Fe	Mn	Al
Content	0.92	0.48	0.04	0.40	0.076	bal.

(298 K, 77 K) and investigated its effect on subsequent NA and PB. It had been found that the introduction of pre-rolling could effectively inhibit the increase in mechanical properties that occurs during NA, leading to a subsequent improvement in BHR. After PB, samples pre-cryorolled at 77 K exhibited greater strength and elongation than those pre-rolled at room temperature.

II. EXPERIMENTAL SETUP AND SIMULATION MODEL

A. *Materials and Procedures*

In this study, Al–Mg–Si alloy sheets with a thickness of 2 mm were used, whose compositions are listed in Table I. Figure 1 shows the experimental flow chart. The sheets were solid solution treated (ST) at 833 K for 30 minutes, followed by water quenching. Then the sheets were immediately pre-cryorolled and room-temperature pre-rolled, with rolling reductions of 5, 10, 15 and 20 pct, respectively. Before cryorolling, the sheets were soaked in liquid nitrogen for 10 minutes. The pre-cryorolled samples were denoted as CR5 pct, CR10 pct, CR15 pct, and CR20 pct, collectively referred to as CR samples; and the room-temperature pre-rolled samples were denoted as RTR5 pct, RTR10 pct, RTR15 pct, and RTR20 pct, collectively referred to as RTR samples. For comparison, one group's samples were not deformed. All pre-rolled samples were kept at room temperature for 2 weeks before being artificially aged at 453 K for 30 minutes to simulate the PB. The abbreviation of different treatment processes is shown in Table II.

The microhardness test was carried out on the HXD-2000TMC/LCD 181101X hardness tester, the load was 20 N, the holding time was 15 seconds, and
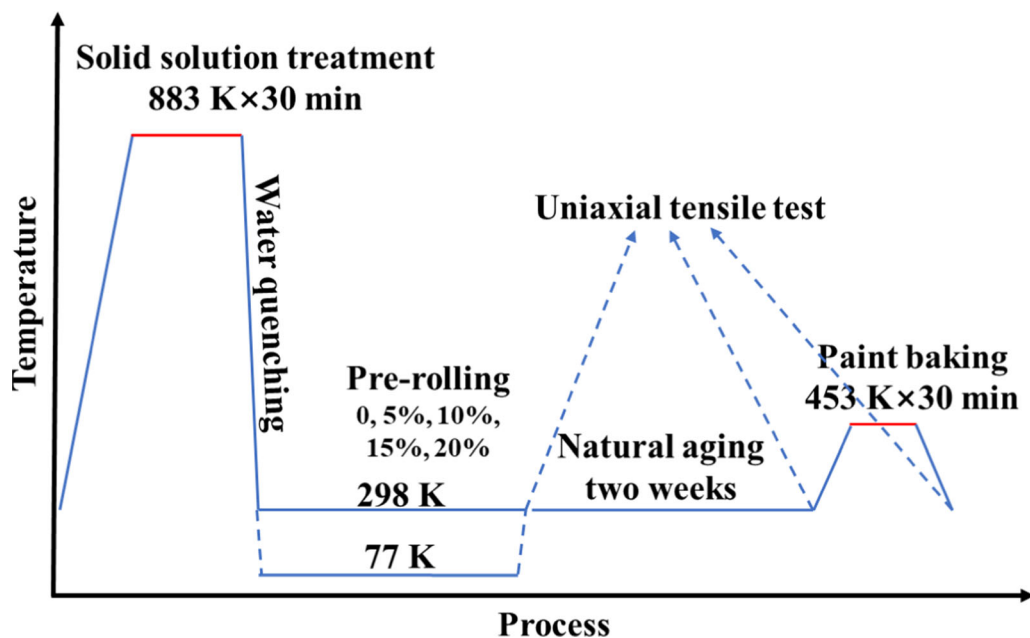

Fig. 1—Schematic of the experimental procedure.

Table II. Abbreviation of Different Treatment Processes

Treatment Process	Abbreviation
Solid Solution Treatment	ST
Solid Solution Treatment + Paint Baking	ST + PB
Solid Solution Treatment + Natural Aging + Paint Baking	ST + NA + PB
Room Temperature Pre-rolling	RTR N pct (N = 5, 10, 15, 20)
Pre-cryorolling	CR N pct (N = 5, 10, 15, 20)
Room Temperature Pre-rolling + Natural Aging	RTR N pct + NA
Room Temperature Pre-rolling + Natural Aging + Paint Baking	RTR N pct + NA + PB
Pre-cryorolling + Natural Aging	CR N pct + NA
Pre-cryorolling + Natural Aging + Paint Baking	CR N pct + NA + PB

at least 7 random test points were tested for each sample. The AGS-X 10-kN test machine was used to conduct uniaxial tensile tests at a tensile rate of 1 mm/min. As shown in Figure 11(d), the tensile sample had a gauge length of 18 mm, a parallel section width of 3 mm, and the length direction was parallel to the rolling direction (RD). Each test was repeated three times under the same condition. Erichsen cupping test compared the formability of different samples. The punch diameter was 20 mm, and the moving speed was 5 mm/min. The test was terminated when the first fracture appeared on the sample's surface.

An optical microscope (OM, MJ42) was used to study the microstructure of samples subjected to ST and pre-rolling. The metallographic samples were cut along the rolling direction-normal direction cross section of the plates, then smoothed with SiC abrasive before being polished mechanically. After electrolytic refining, samples were etched with the Baker reagent (38 ml H_2SO_4, 43 ml H_3PO_4, 19 ml H_2O) and observed under a metallographic microscope. Image J software was utilized to determine the size of 100 grains for every sample. The microstructure of samples was investigated using transmission electron microscope (TEM, FEI Tecnai G2 F20, 200 kV). The main strengthening phase β'' of Al–Mg–Si alloy was in the shape of a small needle parallel to the Al matrix $\langle 100 \rangle$ direction. In order to view the needle precipitates in both cross-section and perpendicular to its length, TEM investigation was done with the Al matrix oriented towards the $\langle 001 \rangle$ regional axis. The TEM sample was mechanically polished to a thickness of less than 0.1 mm, and then wafers with a diameter of 3 mm were prepared using a perforating machine. Finally, the twin jet thinning was carried out in an electrolyte composed of nitric acid and methanol (volume ratio: 3:7). During the thinning process, the temperature was kept in the range of 243 K to 253 K, the voltage was 20 to 30 V, and the current was 80 to 100 mA. D8 ADVANCE Davinci was utilized for XRD tests to analyze phase composition and calculate dislocation density. The scanning rate was 2 deg/min, the scanning step was 0.02 deg, and the range of the angle was 30 to 90 deg. The dislocation density was estimated by XRD tests using the Williamson-Hall method and Jade6 software. Initially, micro-strain e and microcrystal size d are calculated according to the diffraction peak information obtained from the XRD test. Their relationship can be described by Eq. [1]:

$$\frac{\beta \cos\theta}{\lambda} = \frac{1}{d} + 2e\left(\frac{2\sin\theta}{\lambda}\right) \quad [1]$$

where λ is the wavelength, for copper target, λ = 0.15418 nm, θ is Bragg Angle, β is half high width, these two parameters can be obtained directly from the test results. Using $4\sin\theta/\lambda$ and $\beta\cos\theta/\lambda$ as independent and dependent variables, respectively, for linear fitting, the slope and intercept of the fitting line are e and $1/d$. Dislocation density ρ can be calculated by Eq. [2]:

$$\rho = \frac{2\sqrt{3}e}{db} \quad [2]$$

b is the Burgers vector, equal to $a/\sqrt{2}$ for Al, where a is the lattice constant (0.405 nm), then b = 0.286 nm. Scanning electron microscopy (SEM, TESCAN MIRA3 LMU) was used to study the tensile fracture morphology of samples. Electron backscatter diffraction (EBSD) was conducted on the RD-ND(normal direction) plane of samples using an EDAX HIKARI Super field emission scanning electron microscope operated at 15 KV with a step size of 1.5 μm. The samples for EBSD were first mechanical polished and then prepared using an ion milling instrument (IM4000). Differential scanning calorimetry (DSC) was used to analyze the precipitation kinetics of various samples after being stored at room temperature for 2 weeks. The DSC experiments were conducted using TA Q2000 equipment in an argon atmosphere with a temperature range from room temperature to 773 K at a heating rate of 10 K/min.

B. Molecular Dynamics Modeling

In order to study the dynamic change of internal microstructure of the material after pre-rolling with different temperature and reduction, a molecular dynamics (MD) simulation was carried out. The compress deformation behavior of the Al–0.92Mg–0.48Si system at 77 K and 298 K was simulated in LAMMPS with the modified embedded-atom method (MEAM) potential.[26] The model was established by the Voronoi method using the Atomsk software,[27] and the deformation behavior was analyzed by the post-processing software OVITO.[28] The model size was 23.1 nm × 35 nm × 11.55 nm and contained 520186 atoms. According to the mass fraction ratio of different elements, the
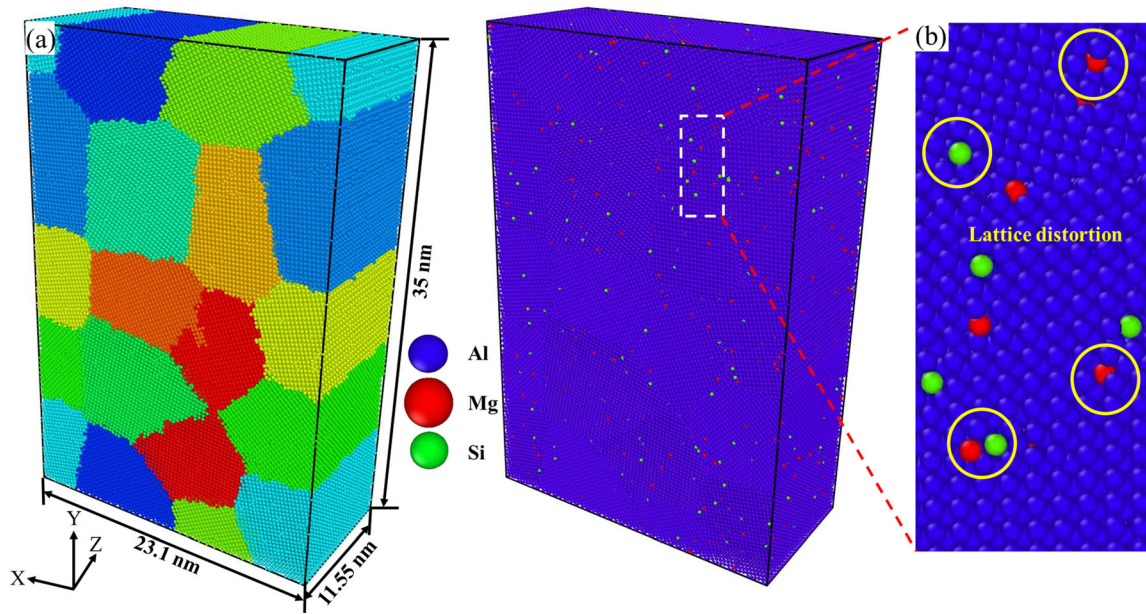
Fig. 2—Molecular dynamics simulation model of (*a*) Al–0.92Mg–0.48Si system and (*b*) lattice distortion in supersaturated solid solution.

atomic ratio of Al, Mg, and Si atoms was set to 98.5, 1.0 and 0.5 pct, respectively. The model consisted of 12 grains, and the compression direction was negative along the *Y*-axis. Periodic boundary conditions were imposed in all three directions. The deformation range was 0 to 20 pct in isobaric-isothermal (NPT) ensemble with a timestep of 0.1 fs. Although shear deformation occurred on the material's surface during the rolling process, this simulation only considered the compression deformation in the thickness direction to simplify the study. The simulation model established by Atomsk is shown in Figure 2(a). Since the pre-deformation was carried out immediately after the solution treatment, the model accurately reflected the lattice distortion in the supersaturated solid solution (Figure 2(b)). The evolution behavior of dislocation under different deformation amount (step size) was observed, and the number and density of dislocations was calculated.

III. RESULTS

A. *Microstructure Characterization*

Figure 3 shows the optical micrograph images of different samples, and their grain size distributions are illustrated in Figure 4. In Figure 3(a), ST sample was consisted of coarse-equiaxed grains with an average about 97.5 μm. In Figures 3(c) through (j), after pre-rolling, the grains underwent elongation along the rolling direction and compression along the thickness direction, resulting the refinement of grains. As seen in Figure 4(b), with the increase of reduction, the mean grain size gradually decreased. For CR and RTR samples, their mean grain size reduced from 88.5 to 62.7 and 91.7 to 67.4 μm when the reduction increased from 5 to 20 pct, respectively. This phenomenon

suggested that the effect of pre-cryorolling on grain refinement was more obvious than room-temperature pre-rolling due to the inhibition of dynamic recovery by cryogenic temperature.

To observe distribution of dislocation and precipitated phase, TEM images of several samples are depicted in Figure 5. Figure 5(a) shows the TEM image of the sample subjected to ST + PB (without NA). It can be seen that a large number of dot-like precipitates were homogeneously distributed in the matrix. According to the high-resolution TEM images shown in Figures 5(b) and (c), the larger dot-like precipitates (measuring 3 to 4 nm) that account for the main part were determined to be β'' phase, while the remaining smaller dot-like precipitates (approximately 2 nm) were identified as GP zone/clusters.[29,30] Without the negative effect of NA, the solute atoms in the matrix could rapidly form a large number of β'' phases. However, when the sample went through NA between ST and PB, as shown in Figure 5(d), a notable reduction in the density of the precipitated phase within the matrix was observed. Only a few dot-shaped GP zones/clusters were present, with minimal transformation into the β'' phase. After the introduction of pre-rolling, as shown in Figure 5(e), exhibits a significant presence of dislocations and dislocation tangles, along with a minor occurrence of dot-shaped clusters within the matrix. According to the HRTEM and corresponding FFT and IFFT images of CR20 pct + NA sample depicted in Figure 5(g) through (i), no clusters or other precipitated phases were observed in the Al matrix, indicating that dislocation introduced by pre-rolling inhibited the formation of clusters during NA. The utilization of dislocation as a heterogeneous nucleation site can enhance the nucleation and growth of precipitated phase, leading to the conversion of the GP region/cluster
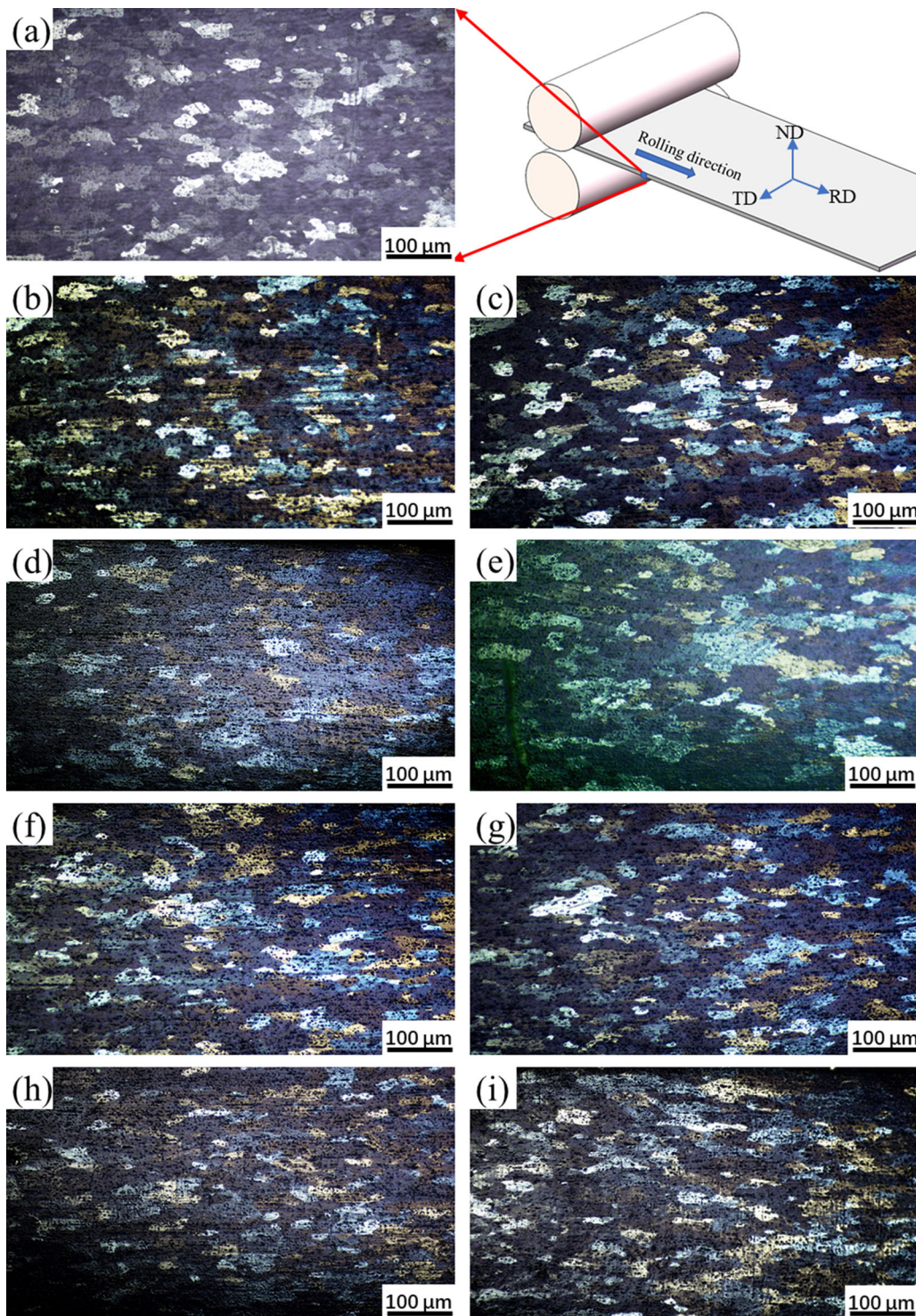
Fig. 3—Optical micrographs for microstructure of samples subjected to (*a*) ST, (*b*) CR5 pct, (*c*) RTR5 pct, (*d*) CR10 pct, (*e*) RTR10 pct, (*f*) CR15 pct, (*g*) RTR15 pct, (*h*) CR20 pct, and (*i*) RTR20 pct.

to the β'' phase and ultimately improving the BHR. Figure 5(f) illustrates that following PB, there was an observable non-uniform distribution of coarse precipitated phases that nucleated along dislocation lines. This phenomenon was not observed in the ST sample. Compared with the precipitated phase in the matrix, the precipitated phase near the dislocation was coarser,

this phenomenon can be attributed to two reasons. First, the Al lattice around dislocation was usually distorted and had a large elastic strain energy, so precipitation nucleation and growth resistance along the dislocation will be reduced compared to the Al matrix. Second, solute atoms have a higher diffusion rate in close proximity to the dislocation. Due to dislocation
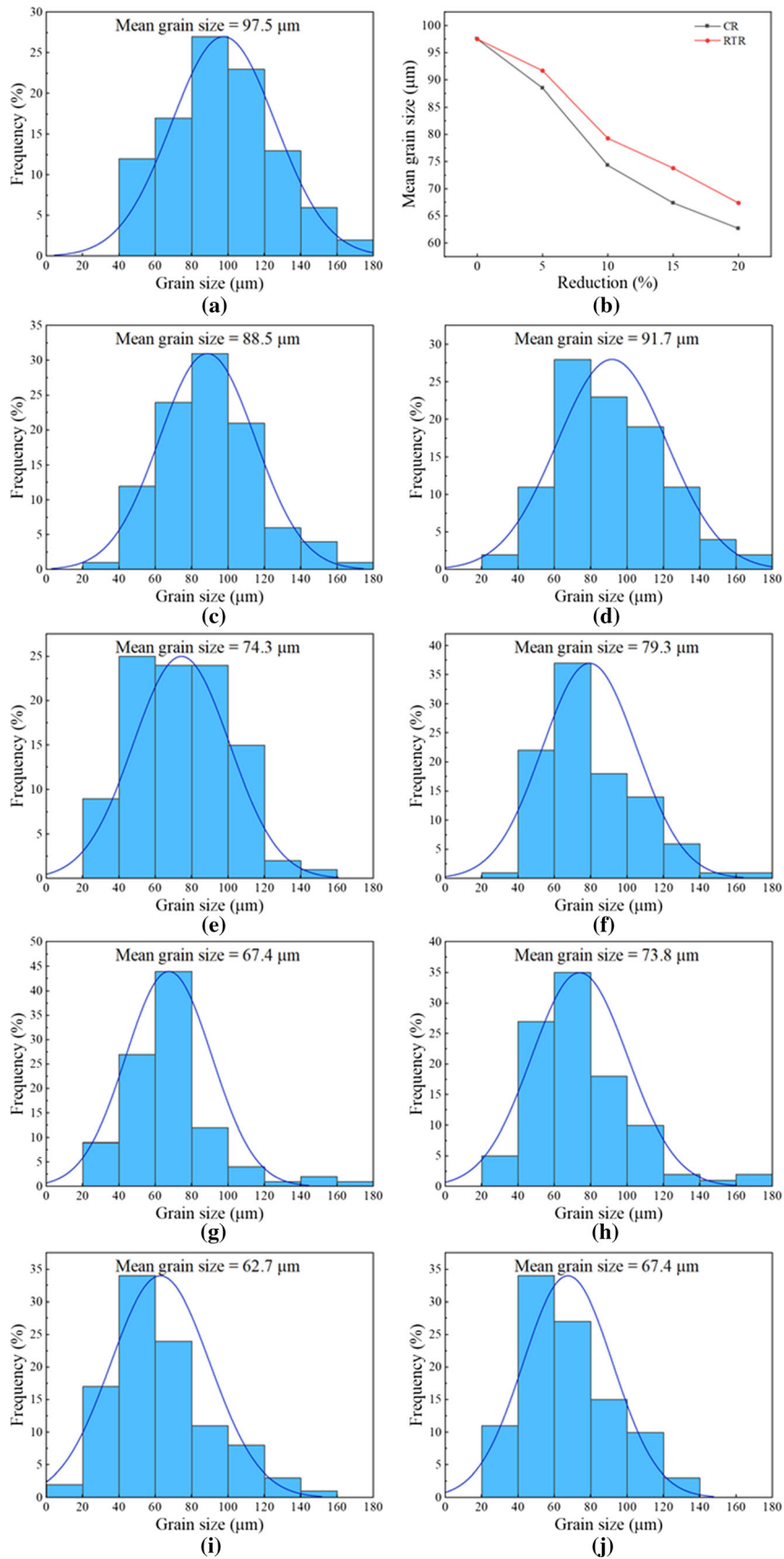
Fig. 4—Grain size distribution of samples subjected to (*a*) ST, (*c*) CR5 pct, (*d*) RTR5 pct, (*e*) CR10 pct, (*f*) RTR10 pct, (*g*) CR15 pct, (*h*) RTR15 pct, (*i*) CR20 pct, (*j*) RTR20 pct. (*b*) Relationship between mean grain size and reduction.
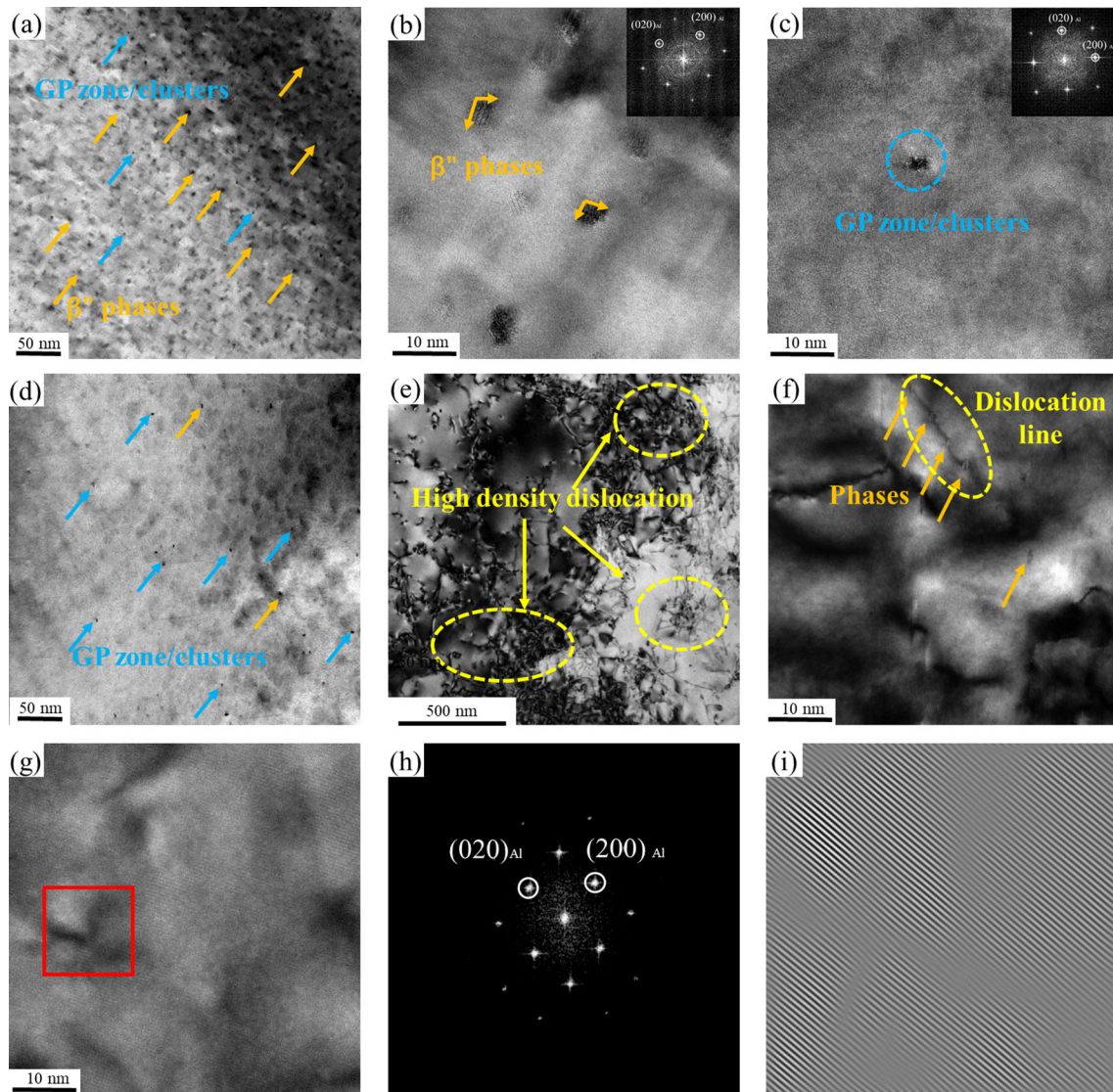
Fig. 5—TEM Bright field images of samples. (*a*) ST + PB sample, (*b*) and (*c*) HRTEM image and corresponding FFT images of β'' and GP zone/Cluster in (a), (*d*) ST + NA + PB sample, (*e*) CR20 pct + NA sample, (*f*) CR20 pct + NA + PB sample, (*g*) HRTEM image of (e), (*h*) and (*i*) FFT and IFFT images of the red rectangular region in (g) (Color figure online).

entanglement, it is difficult to observe a clear β'' phase structure in CR20 pct + NA + PB sample.

Figure 6 shows the XRD diffraction patterns of ST, CR15 pct and RTR15 pct samples before and after PB. The number and location of diffraction peaks in different samples were basically the same, but the intensity of peaks varied greatly. The plane (200) exhibited the maximum diffraction intensity among all the samples. In the ST sample, the intensity of (111) and (311) planes were very low. After pre-rolling, the intensity of these two planes increased noticeably, and the peak of (200) plane shifted to the left as shown in Figure 6(b), indicating that pre-rolling led to lattice distortion and a slight increase in the lattice constant. The increase in peak width represented that the pre-rolling made the grain size fine. In the RTR15 pct sample, it was observed that the diffraction intensity of all main peaks exhibited an increase after PB. Conversely, in the CR15 pct sample, the intensity of the

(111) plane remained relatively constant, while the intensity of the (200) plane increased. However, the intensity of the (220) and (311) planes experienced a slight decrease.

The microstrain, microcrystal size and dislocation density of samples are shown in Table III Before PB, the ST + NA sample's dislocation density was the lowest, 0.78×10^{13} m^{-2}, the CR15 pct + NA sample's showed the highest dislocation density, which was 10.1×10^{13} m^{-2}, 16.1 pct higher than that of RTR15 pct + NA sample. Increasing the dislocation density may potentially enhance the BHR to a greater extent and have been verified by mechanical properties experiment in next section. Recovery happened in PB resulting in the decrease of dislocation density, the dislocation density of CR15 pct + NA + PB and RTR15 pct + NA + PB samples were reduced to 9.1×10^{13} m^{-2} and 8.0×10^{13} m^{-2}, respectively.
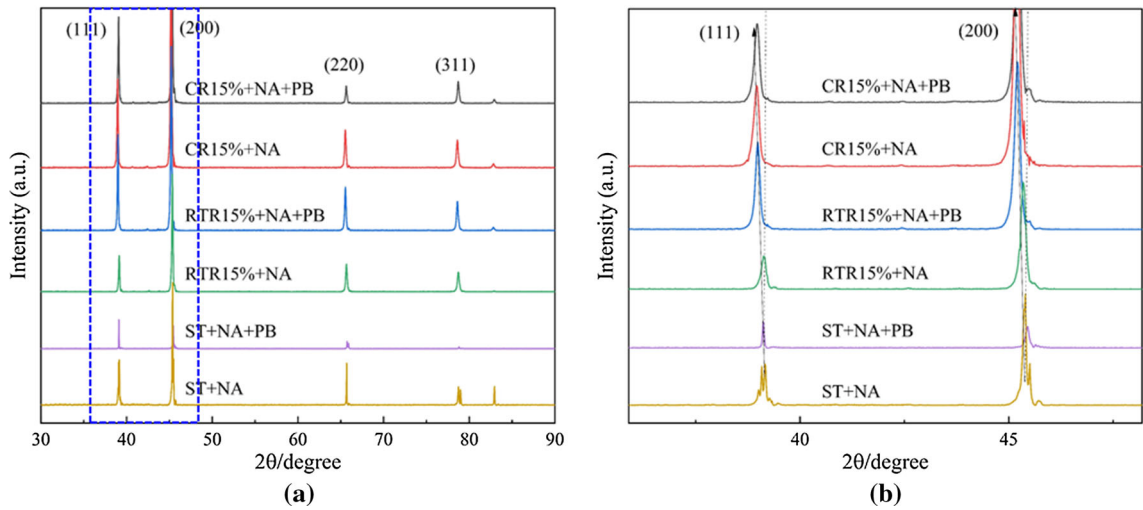
Fig. 6—(a) XRD patterns of ST, CR15 pct and RTR15 pct samples before and after PB, (b) Local amplification of the blue rectangle in (a) (Color figure online).

Table III. Dislocation Density of ST, CR15 Pct, and RTR15 Pct Samples Before and After PB

Sample	Micro-crystallite Size d, (nm)	Micro-strain e, ($\times 10^{-3}$)	Dislocation Density ρ, ($\times 10^{13}$ m^{-2})
ST + NA	248.4	0.016	0.78
ST + NA + PB	265.7	0.015	0.69
CR15 Pct + NA	91.4	0.77	10.1
CR15 Pct + NA + PB	96.8	0.73	9.1
RTR15 Pct + NA	115.0	0.82	8.7
RTR15 Pct + NA + PB	169.5	1.12	8.0

B. *Microstructure and Dislocation Evolution of Nanoscale Al–0.92Mg–0.48Si System During Compress Deformation*

The structure evolution and dislocation behaviors in the material after compress deformation with different temperatures and reductions were studied by molecular dynamics simulation. The structure evolution in two temperatures vary with engineering strain ε are shown in Figures 7(a) and (b). During the compress deformation, the face-centered cube (FCC) structure of Al matrix was gradually replaced by a hexagonal close-packed (HCP) structure. The lamellar HCP structure parallel to each other was considered as stacking faults (SFs) formed by dislocation slip. The quantity of SFs exhibited a swift rise when ε was between 5 and 10 pct, followed by a decline during the final stages of deformation. This trend is further confirmed by the variation tendency of dislocations shown in Figure 20(a). It is obviously that the number of SFs in the model subjected to deformation at 77 K was higher than that observed at 298 K, suggesting an increased dislocation density at cryogenic temperatures. Figures 7(c) and (d) provide a localized perspective when viewed along the X-axis. The present findings indicated that the orientation of the SFs was at an angle of 45 and 135 deg relative to the compression direction. This observation is in agreement with the established correlation between the shear direction and loading direction in macroscopic deformation.

As shown in Figure 8, after the models relaxed at corresponding temperature (77 K and 298 K), dislocations were predominantly located at grain boundaries to achieve grain boundary adaptation, and the main type was perfect dislocation. A small number of dislocation rings existed in the matrix, which was Shockley partial dislocation. The number of perfect dislocations near grain boundaries in the model relaxed at 298 K was less than that at 77 K (black ellipse in Figure 8), and they quickly transformed into Shockley partial dislocation during subsequent compress deformation. When the engineering strain was 5 pct, perfect dislocations near the grain boundary were still relatively complete in the model deformed at 77 K, but almost disappeared at 298 K. At the initial stage of deformation, the dislocation nucleated inside the grains and gradually developed into a Shockley partial dislocation ring. At the same time, perfect dislocation gradually reduced. When the engineering strain increased to 7 pct, another dislocation nucleation mechanism appeared, originating from a single point and exhibiting divergent growth. The dislocation content reached saturation when the engineering strain was 10 pct, and then gradually decreased as the engineering strain continued to increase. Finally, all dislocations appeared to be broken, the dislocation line length became shorter, and perfect dislocations almost completely disappeared. The observed decrease in dislocation density aligns with the findings of
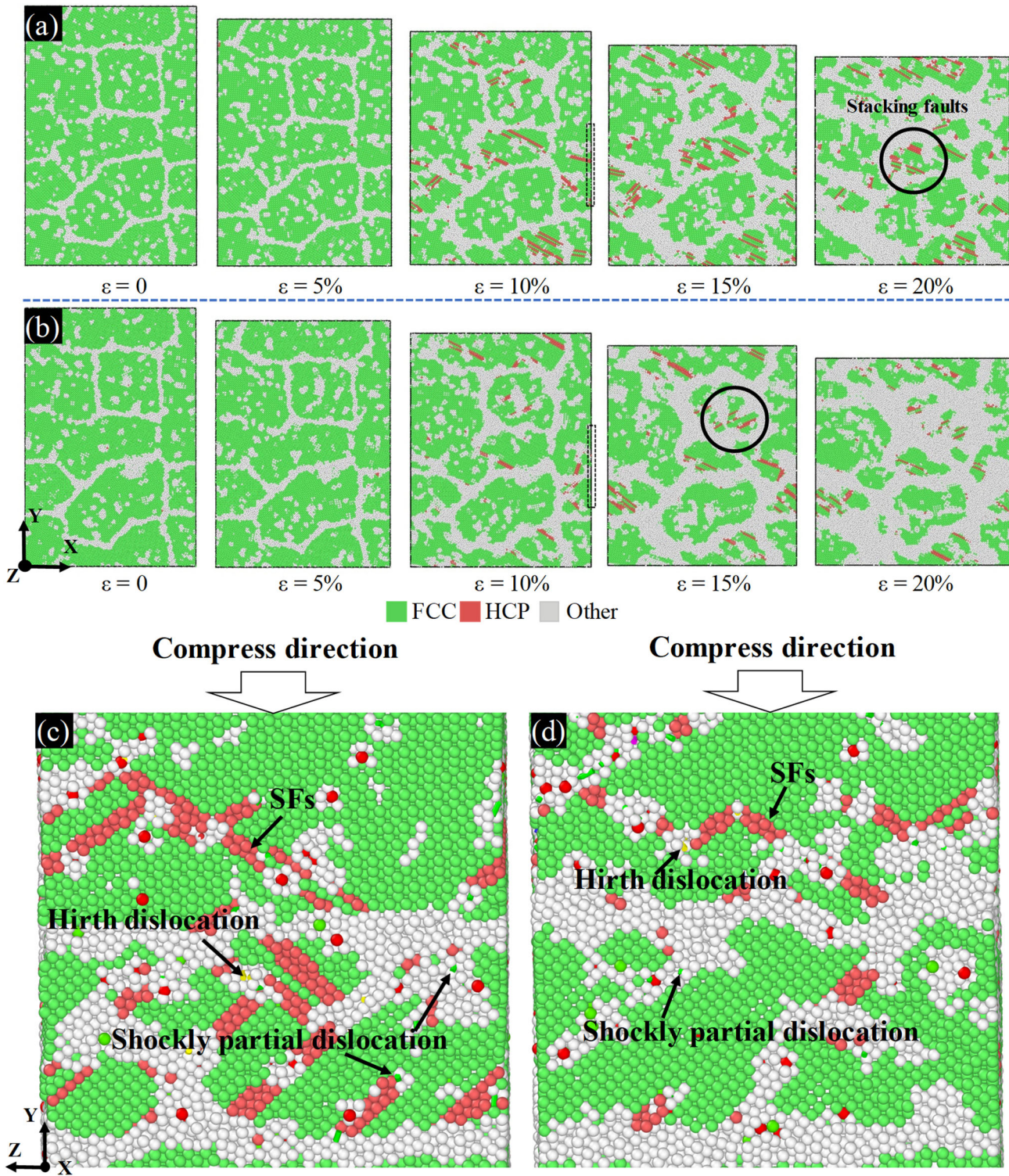
Fig. 7—Microstructure evolution varying with engineering strain in MD simulation (*a*) 77 K, (*b*) 298 K, (*c*) and (*d*) are the local magnification of side view in (*a*) and (*b*) with engineering strain $\varepsilon = 10$ pct (dotted rectangular region), respectively.

previous researchers.[31] In the small system, dislocation easily slips out of the free plane of samples, causing the dislocation annihilation rate to be even higher than their nucleation rate. Consequently, the dislocation density gradually reduces and eventually attains a state of "hunger" during the deformation process. Subsequent

plastic deformation necessitates the application of supplementary external loads to initiate the formation of a new dislocation. Since cryogenic temperature inhibited dislocation motion and slowed down its annihilation rate of slip out of the surface, the dislocation density in the model deformed at 77 K was higher than that at 298
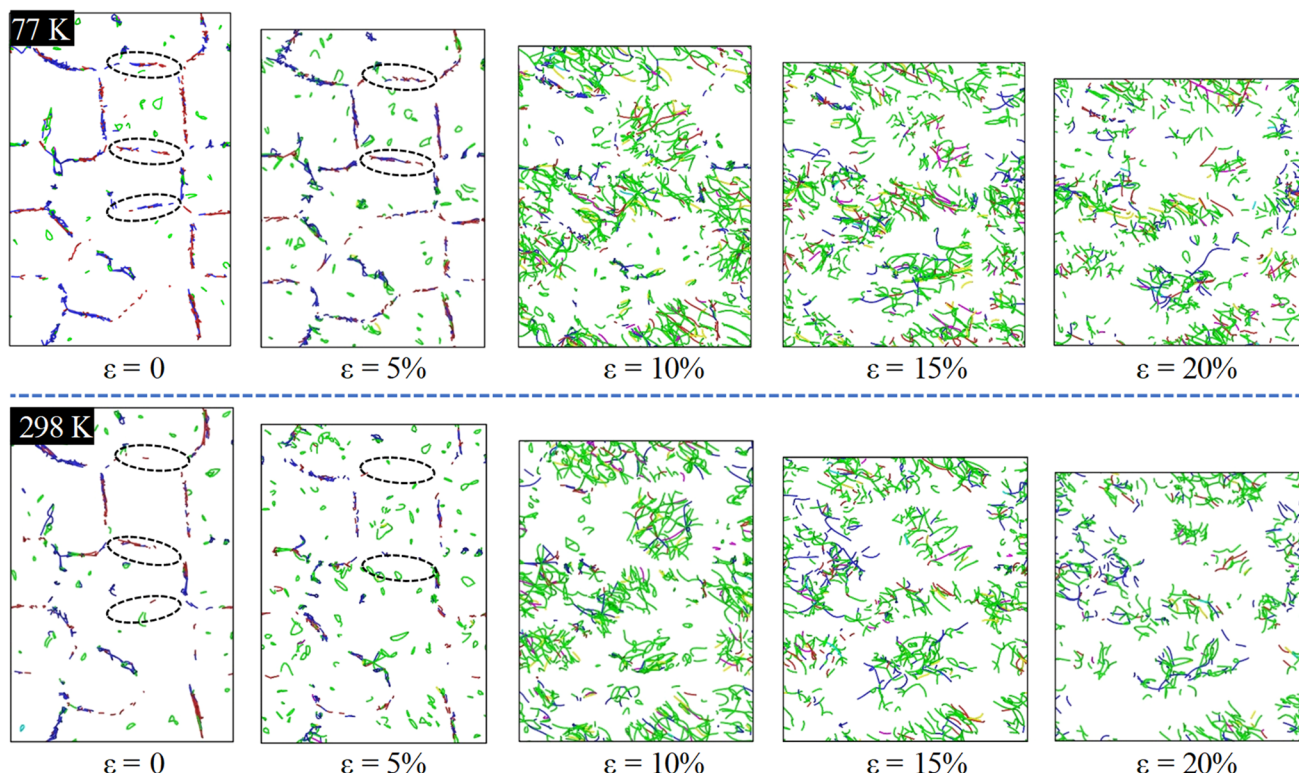
Fig. 8—Snapshot of dislocation evolution of 77 K and 298 K compression deformation by MD simulation. The blue, green, red, and yellow lines represent perfect dislocation, Shockly partial dislocation, other dislocation, and Hirth dislocation, respectively (Color figure online).

K during the stage when dislocation density began to decrease.

In order to further observe the growth and annihilation of dislocation, local areas of the model were studied and snapshots with representative time steps were selected, as shown in Figure 9. When the engineering was less than 2 pct, the length of the perfect dislocation near the grain boundary was large. After compression loading, the model deformed and the perfect dislocation split into Shockley partial dislocation. Shockley partial dislocation could then merge and form perfect dislocation. Simultaneous and repeated splitting and merging processes resulted in a gradual increase in the proportion of Shockley partial dislocations and a corresponding decrease in the proportion of perfect dislocations. This continued until the length of dislocation line was reduced to a significant extent (ε = 5 pct). At a temperature of 298 K, the model exhibited a higher rate of perfect dislocation splitting into Shockley partial dislocation, while the rate of Shockley partial dislocation merging into perfect dislocation was lower than 77 K, resulting in a rapid increase of Shockley partial dislocation density during the initial stage of deformation. When ε was 5.5 pct, Hirth dislocation appeared in the system, and the dislocation entanglement was more obvious as shown in the black circle in Figure 9. When ε was 15 pct, various dislocations coexisted and appeared to be broken, dislocation line length was short, showing a dispersed distribution. Dislocation density was further reduced at the end of deformation (ε = 20 pct). However, it was noted that the model deformed at 77

K exhibited a higher dislocation density than at 298 K. The dislocation density and type evolution during simulate deformation in LAMMPS are analyzed by the Dislocation analysis (DXA) module in OVITO. Shockley partial dislocation and perfect dislocation are two major parts of the total dislocation and their changing trends are shown in Figure 10. Since the stair-rod dislocations, Hirth dislocations, and Frank dislocations contributed less, they were added to the total dislocation and not counted alone. As described in Figure 10, when the ε is 5, 10, 15 and 20 pct (corresponding to the four reductions of the macroscopic pre-rolling process), the total dislocation densities of the model deformed at 77 K are higher than these of the model deformed at 298 K. In particular, when the ε is 15 pct, the total dislocation density is 18.3 pct higher, which is close to the 16.1 pct calculated by XRD experiment in Table III

C. Mechanical Properties

1. Age-hardening behavior

The hardness changes of each group of samples during the whole process of NA for 2 weeks and subsequent PB were recorded. As shown in Figure 11(a), the hardness of all samples exhibited the same variation trend, which increased significantly on the first day after ST and pre-rolling, and then maintained a slight fluctuation in the NA within 2 weeks. After PB at 453 K × 30 minutes, the hardness increased again in different degrees. The hardness change of
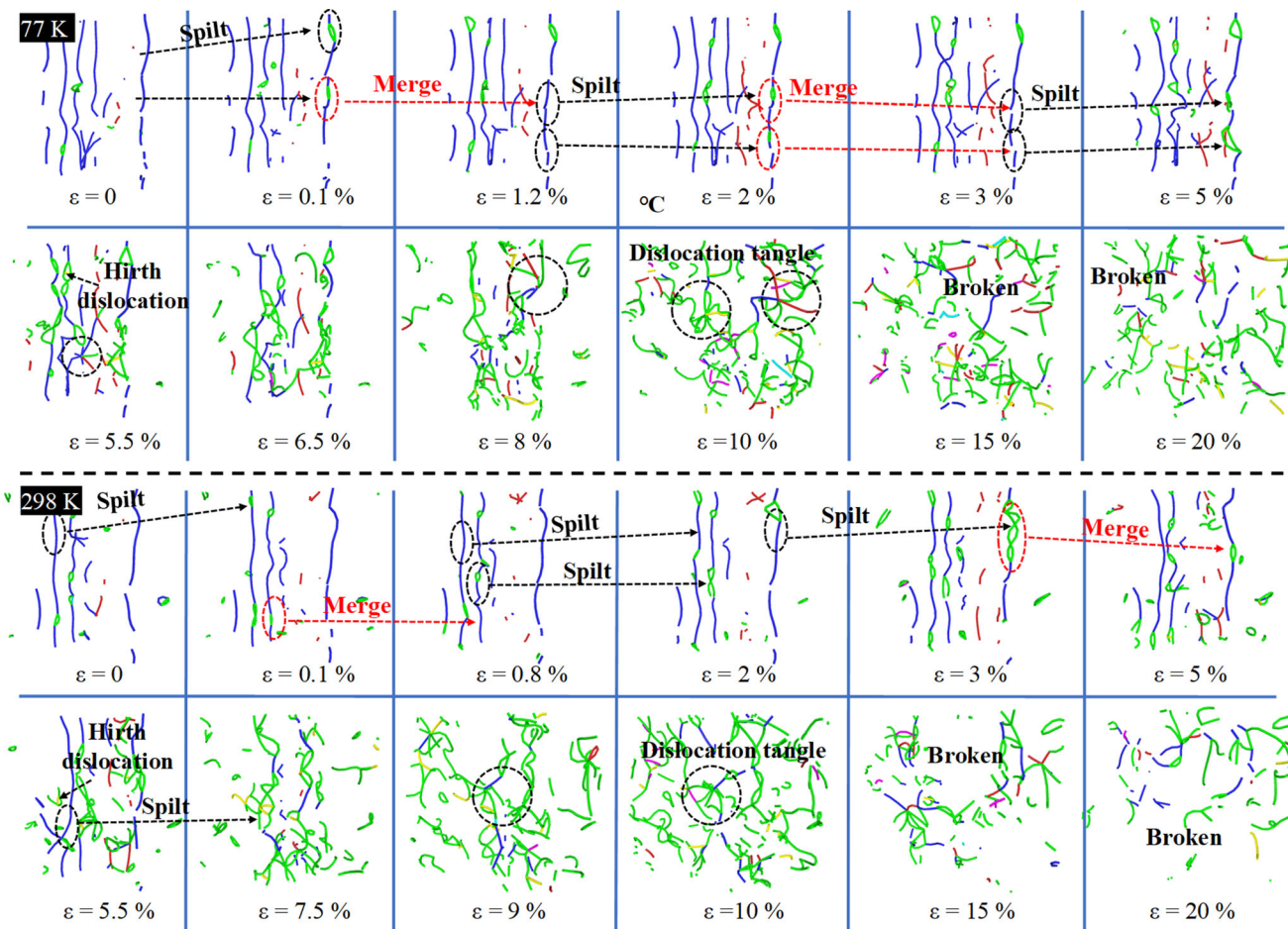
Fig. 9—Snapshot of local dislocation evolution of 77 K and 298 K compression deformation by MD simulation.
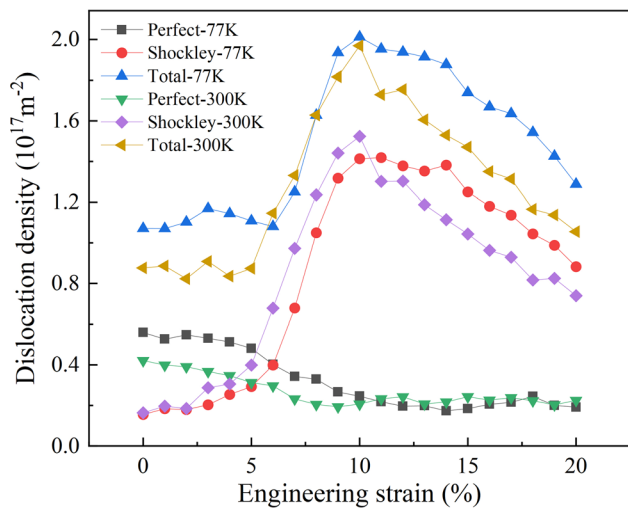

Fig. 10—Evolution of dislocation density ρ at 77 K and 298 K.

samples in different stages was counted and shown in Figure 11(b) and Table IV. The ST sample without pre-rolling exhibited an increase from 56.6 to 83.8 HV over 2 weeks of NA, followed by a further rise to 90.3 HV after PB. The BHR was only 6.5 HV, which was significantly lower than the BHR of ST + PB sample (55.4 HV, the red rectangle in Figure 7(a)), indicating that NA had a severe negative effect on the BHR, causing an adverse influence on the anti-sag property of the sheets in service. After the introduction of pre-rolling, the deformed samples exhibited a notable increase in hardness of approximately 20 to 30 HV compared to the ST sample, attributable to work hardening. Simultaneously, there was a significant decrease in the hardness increase during the NA stage, which declined from 27.2 HV to approximately 15 HV. Their BHR was improved to over 10 HV and increased proportionally with the degree of reduction. Specifically, from 9.6 HV of CR5 pct sample to 16.3 HV of CR20 pct sample. The influence of room-temperature pre-rolling on hardness was similar to that of pre-cryorolling, but the hardness and BHR of RTR samples were slightly lower than those of CR samples when subjected to the same level of reduction. The largest BHR and hardness following PB were obtained in CR20 pct sample, measuring at 16.3 HV and 116.4 HV, respectively.

2. Tensile properties

To investigate the impact of pre-rolling on tensile properties, samples were taken at three distinct stages, as illustrated in Figure 1. These stages include after
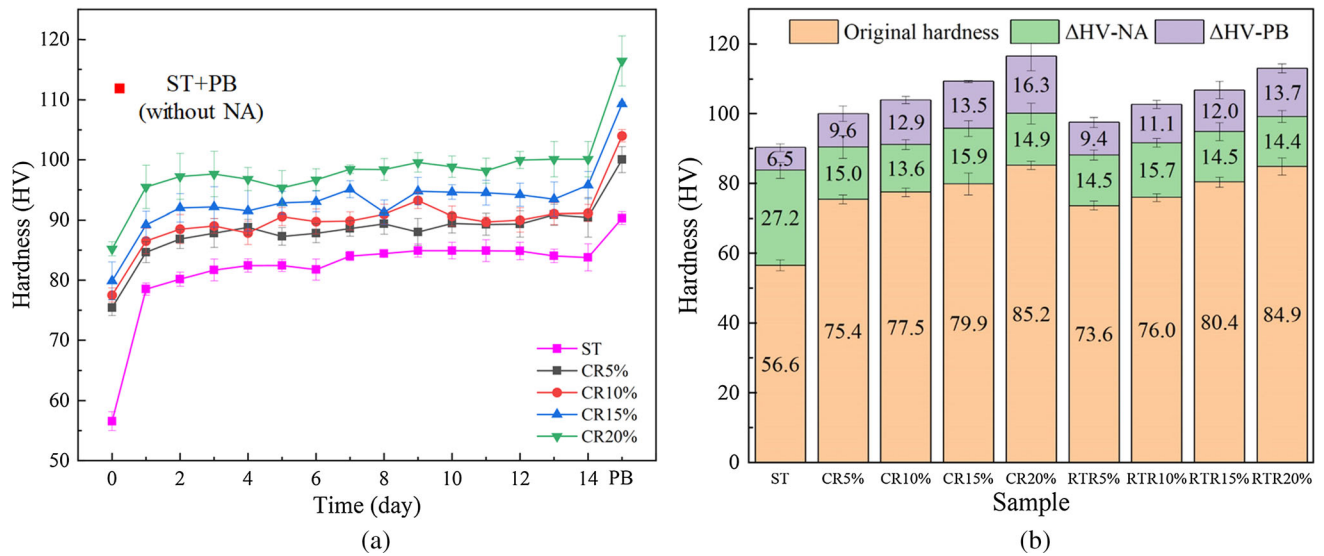
Fig. 11—(*a*) hardness curve during NA and subsequent PB, (*b*) Hardness change(ΔHV) in different stages.

Table IV. Hardness Changes (ΔHV) of Different Samples During NA and PB

Sample	Before NA (Original)	After NA	After PB	ΔHV in NA	ΔHV in PB (BHR)
ST	56.6 ± 1.6	83.8 ± 2.3	90.3 ± 1.1	27.2	6.5
CR5 Pct	75.4 ± 1.3	90.4 ± 3.3	100.0 ± 2.2	15.0	9.6
CR10 Pct	77.5 ± 1.2	91.1 ± 1.4	104.0 ± 1.0	13.6	12.9
CR15 Pct	79.9 ± 3.1	95.8 ± 2.2	109.3 ± 0.3	15.9	13.5
CR20 Pct	85.2 ± 1.2	100.1 ± 3.0	116.4 ± 4.1	14.9	16.3
RTR5 Pct	73.6 ± 1.3	88.2 ± 1.4	97.6 ± 1.4	14.6	9.4
RTR10 Pct	76.0 ± 1.1	91.7 ± 1.2	102.7 ± 1.2	15.7	11.1
RTR15 Pct	80.4 ± 1.5	94.9 ± 2.5	106.9 ± 2.5	14.5	12.0
RTR20 Pct	84.9 ± 2.5	99.2 ± 1.7	112.9 ± 1.3	14.4	13.7

pre-rolling (before NA), after 2 weeks of NA, and post-precipitation hardening (after PB). Uniaxial tensile tests were subsequently conducted on the samples at room temperature, with the dimensions of the uniaxial tensile sample depicted in Figure 12(d). The engineering stress-strain curves are shown in Figures 12(a) through (c) and yield strength (YS), ultimate tensile strength (UTS), uniform elongation (UE) and total elongation (TE) are listed in Figure 13. Before NA, the YS of ST sample was only 102.8 MPa and it was significantly improved through pre-rolling. For CR5 pct sample, the YS was 178.2 MPa, indicating a significant increase of 73.3 pct. The YS exhibited an upward trend in response to the rolling reduction increase. When the reduction was 20 pct, the YS of CR20 pct and RTR20 pct samples were 237.9 and 231.9 MPa, respectively. The variation trend of UTS was different from YS. Under 5 and 10 pct reductions, the pre-rolling would reduce the UTS of samples. Only when the reduction increased to 15 pct would the UTS of the pre-rolled samples higher than that of ST sample again, and this trend maintained until the end of NA. Overall, the YS and UTS of CR samples were about 5 MPa higher than that of RTR samples, while the elongation was about 1 pct lower. After 2 weeks of NA, the YS and UTS of all samples

increased. The YS of ST sample rose 37.3 MPa, while the YS increment of pre-rolled samples was within 15 MPa, indicating that pre-rolling inhibited the precipitation during NA. At the same time, the UTS of the ST sample also increased the most among all samples, which was 30.2 MPa. This result was consistent with the maximum hardness increment for the ST sample in NA stage. After PB, the tensile strength was further improved. The YS and UTS of ST sample only increased by 8.5 and 6.2 MPa, respectively. In contrast, the pre-rolled samples demonstrated a greater increase in YS and UTS, exceeding 10 and 20 MPa. The UTS of CR20 pct sample increased by 42.2 MPa, which was 5.8 times higher than the ΔUTS of ST sample, the highest among all samples. In the process of driving, the requirements of car body plate are anti-sag performance and shock absorption ability. The primary objective is to ensure the YS, followed by UTS and resistance to fracture. The YS of ST sample after PB was only 148.6 MPa, but it could increase by 36 to 80 pct through pre-rolling, with the cost of decreasing elongation. The YS and UTS of CR samples after PB was 5 to 10 MPa higher than that of RTR samples, and the total elongation was also higher. These results show that pre-cryorolling is an effective pre-treatment process for
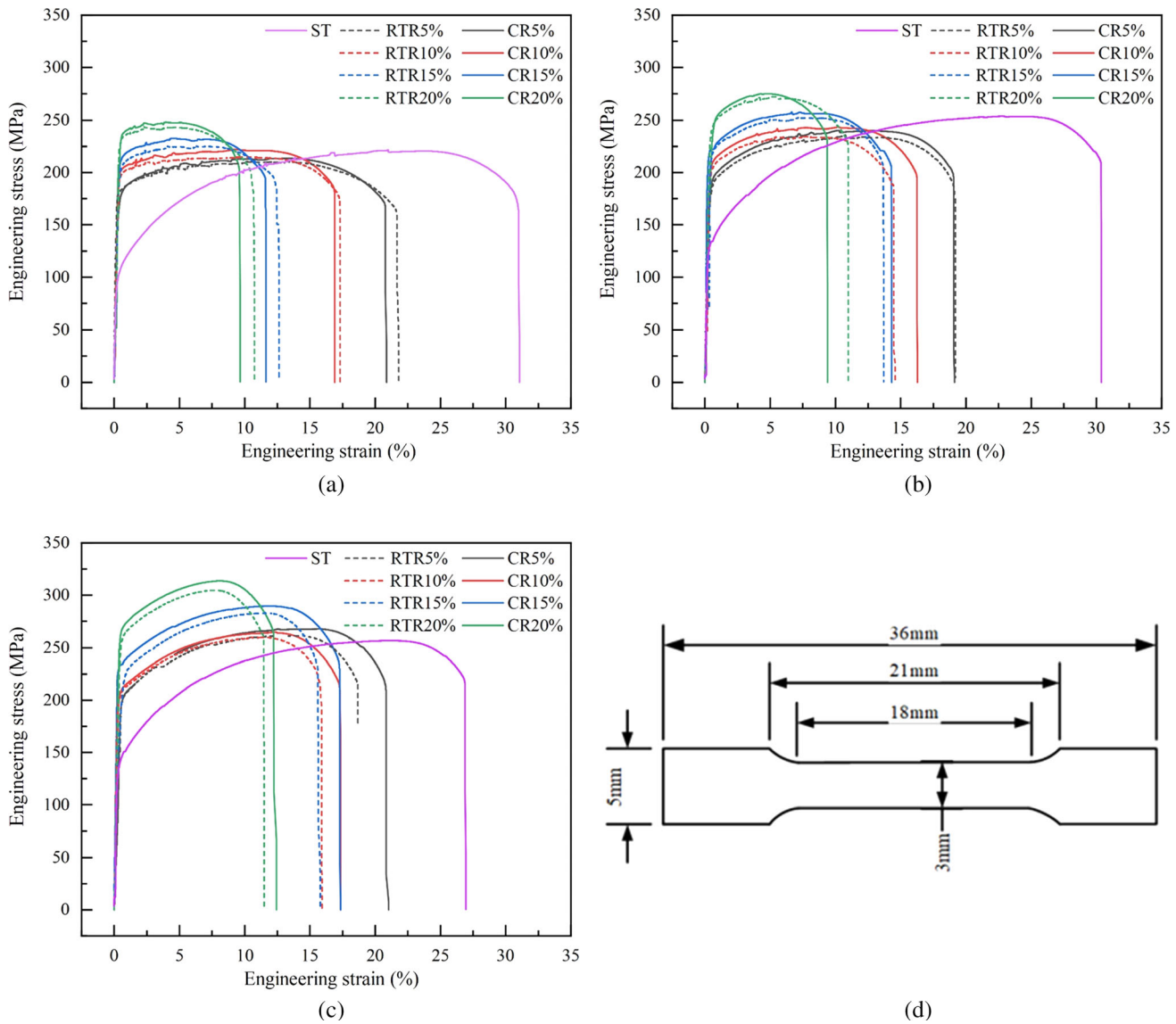
Fig. 12—Engineering stress-strain curves of samples in different stages. (*a*) before NA, (*b*) after NA, (*c*) after PB, (*d*) size of uniaxial tensile sample.

Al–Mg–Si alloys. Furthermore, as depicted in Figures 13(a) and (b), the increase in UTS was observed to be greater than that of YS during both NA and PB processes for pre-rolled samples. This suggests an enhancement in work hardening capacity, which will be further expounded upon in the subsequent discussion segment.

In contrast to the monotonic increase of YS and UTS during NA and PB, it can be seen in Figure 13(c) that the change of elongation was more complex. The initial TE of ST sample was 31.0 pct. After 2 weeks of NA, it was reduced to 27.6 pct. After PB, it was reduced again by 1.9 pct, showing a decreasing trend. While the TE of pre-rolled sample decreased or was almost unchanged at the NA stage, only the TE of CR15 pct sample increased by 3.4 pct, which was beneficial for formability. After PB, most pre-rolled samples' TE increased within the range of 1.2 to 3.3 pct, only a decrease of 0.9 pct for RTR5 pct sample. Therefore, it can be inferred that the

TE of pre-rolled samples underwent a slight increase during PB. As illustrated in Figure 13(d), the difference in UE between different groups of samples was more pronounced. The UE of ST samples exhibited an initial increase followed by a subsequent decrease during the NA and PB stages, ultimately maintaining the highest value among all samples. The UE of CR10 pct, CR15 pct, CR20 pct, RTR15 pct and RTR20 pct samples increased monotonically, while the UE of CR5 pct, RTR5 pct and RTR10 pct samples decreased first and then increased. The high uniform elongation helps to ensure the uniformity of deformation in the stamping forming process, thereby preventing severe uneven thickness distribution or sheet breakage.

3. Tensile fracture morphology

Figure 14 shows the SEM images of tensile fracture morphology of ST, RTR15 pct and CR15 pct samples at three stages: before NA, after NA, and after PB. The
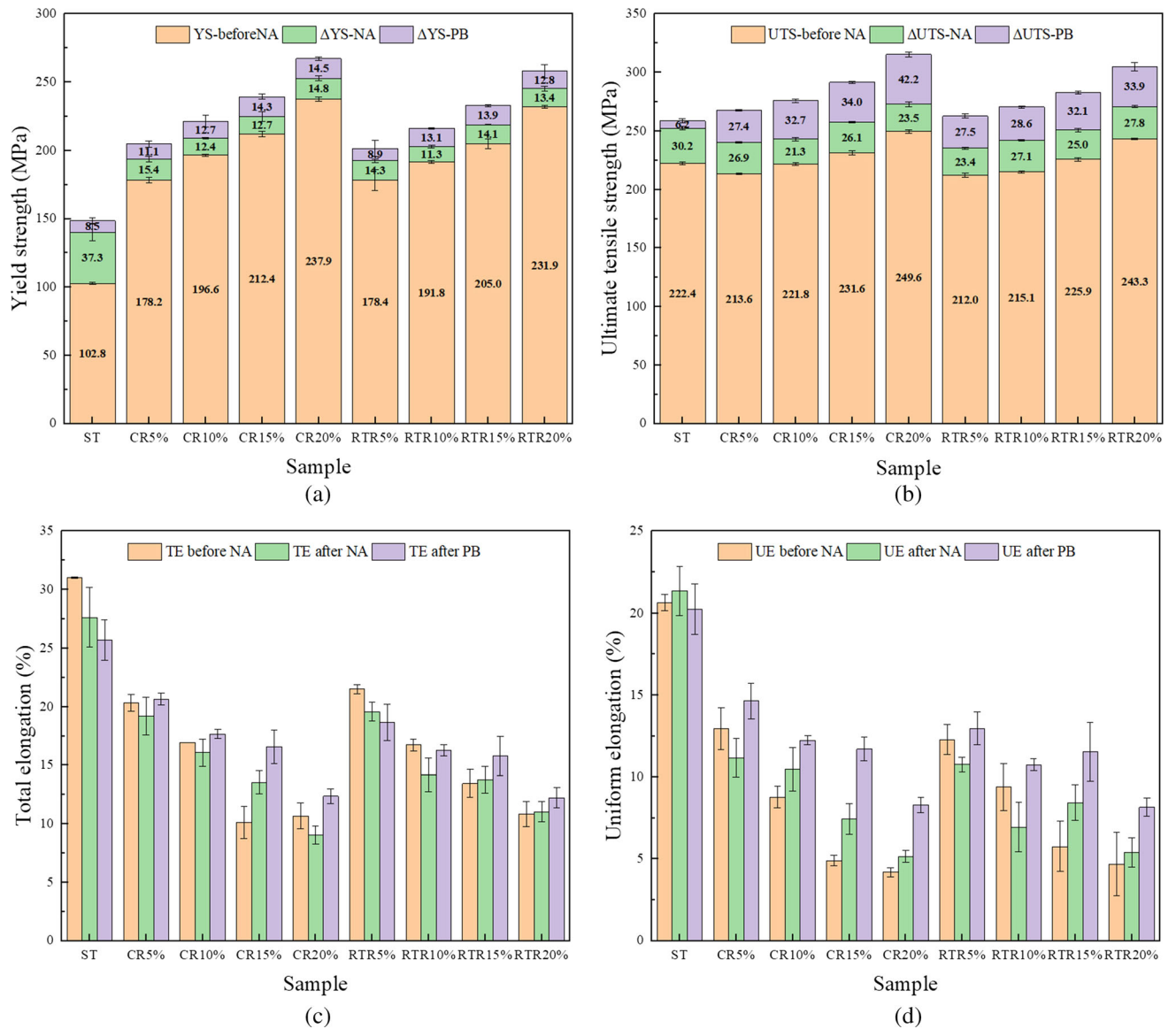
Fig. 13—Schematic diagram of samples' tensile properties. (*a*) yield strength (YS), (*b*) ultimate tensile strength (UTS), (*c*) total elongation (TE), (*d*) uniform elongation (UE).

morphology of the ST sample exhibited a significant number of dimples, as evidenced by Figure 14(a). These dimples were characterized by their substantial size and depth, which is in line with the sample's highest total elongation. The fracture mechanism is attributed to transgranular fracture induced by dimples. After pre-rolling was introduced, the size and depth of fracture dimples decreased with the reduction increase, and cleavage planes appeared in some areas Figures 14(b) and (c). The predominant fracture mode observed is a transgranular fracture, accompanied by a minor occurrence of intergranular fracture. After NA, the three groups of samples showed little change in dimple size, but small particles appeared at the bottom of some dimples, as shown by the pink arrows in Figures 14(d) through (f). These particles are hard phases precipitated during the NA stage. During stretching, the positioning of particles may serve as a source for crack initiation or

propagation path. This is a contributing factor to the sensitivity of fracture resistance and elongation of heat-treated aluminum alloy to the quantity and distribution of precipitated phases.[32] The number of particles in the fracture zone of ST sample was significantly higher than that of RTR15 pct and CR15 pct samples, indicating the spontaneous precipitation during the NA stage was more obvious in the sample without pre-treatment, and pre-rolling could effectively inhibit such precipitation. For RTR15 pct and CR15 pct samples, the presence of particles improved their tensile strength and elongation. After PB, the dimple morphology of all samples had changed, small dimples were nested in large dimples, as shown in Figures 14(g) through (i), and there were still some particles in the dimples, it is presumed to be the strengthening phase precipitated in the PB process. The number of large dimples of ST sample decreased, but increased in CR15 pct and RTR15 pct
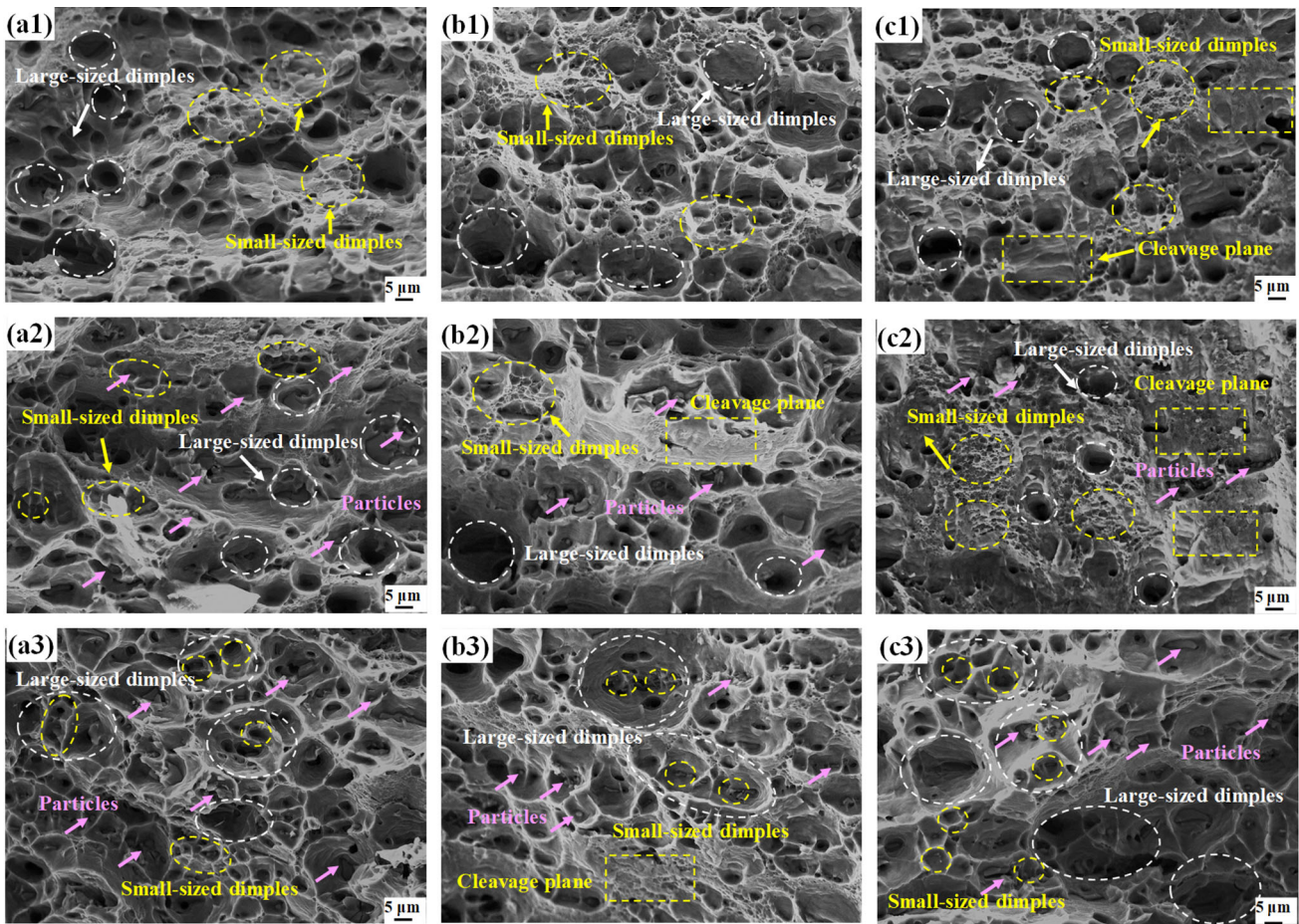
Fig. 14—Fracture morphology of samples in different states. (a1) through (a3): ST sample before NA, after NA, after PB, (b1) through (b3): RTR15 pct sample before NA, after NA, after PB, (c1) through (c3): CR15 pct sample before NA, after NA, after PB.
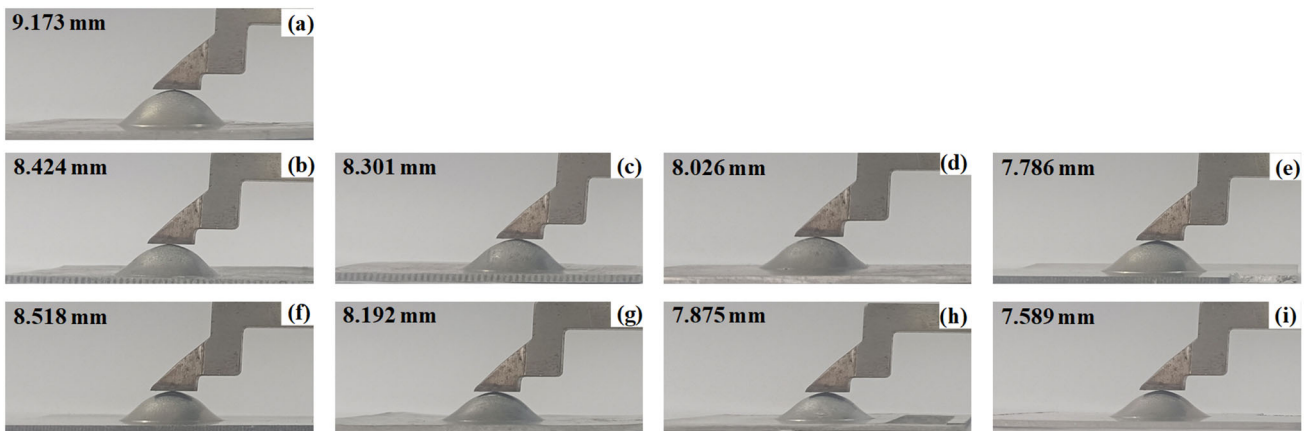

Fig. 15—Cupping photos of: (a) ST, (b) CR5 pct, (c) CR10 pct, (d) CR15 pct, (e) CR20 pct, (f) RTR5 pct, (g) RTR10 pct, (h) RTR15 pct, and (i) RTR20 pct samples.

samples. The number of large dimples in CR15 pct sample was higher than that in RTR15 pct sample, indicating better plasticity and consistent with their change of total elongation in Figure 13(c).

4. *Formability of pre-rolled plates*

In order to compare the influence of different pre-rolling treatments on the formability of the alloy, the Erichsen cupping test was carried out on the samples after 2 weeks of NA. Erichsen cupping test is a commonly used test method to determine the
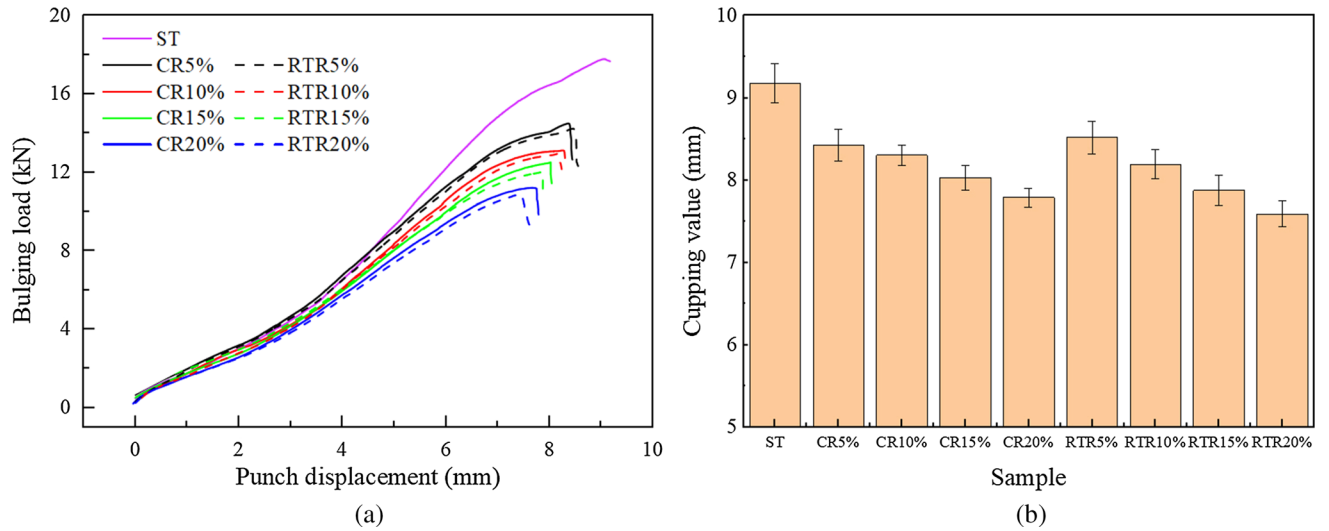
Fig. 16—Erichsen cupping test curves (*a*) and cupping values (*b*) for each group of samples.

formability of a metal sheet, in which a specified steel ball or ball punch is used to press a sample into a concave die until a crack is produced. At this time, the displacement of punch is called "cupping value", the larger the cupping value, the better the material's formability. Figures 15 and 16 depict the samples following the cupping test and the corresponding experimental outcomes. Figure 16(a) illustrates that the bulging force gradually increased as the punch move distance increased. The bulging force of samples in each group was similar when the displacement was below 4 mm. As the punch's displacement increased, the bulging force discrepancy also grew. The results indicate that the ST sample exhibited superior formability and the highest breaking force, as evidenced by its cupping value of 9.2 mm and breaking force of 17.8 kN. Following the introduction of pre-rolling, there was a reduction in both the cupping value and breaking force. For CR samples, when the reduction increased from 5 to 20 pct, the breaking force decreased from 14.4 to 11.3 kN, and the cupping value decreased from 8.4 to 7.8 mm. In Figure 16(b), the cupping value of RTR5 pct sample was similar with that of CR5 pct sample. However, when the reduction increased to be more than 10 pct, the cupping value and breaking force of CR samples were gradually higher than that of RTR samples, and their difference became larger with the increase of reduction.

IV. DISCUSSION

A. *Effect of NA and PB on Work Hardening Ability and Tensile Strength*

According to Figure 12, it can be seen that the difference between UTS and YS of the samples became gradually larger after NA and PB, the slope of engineering stress strain curves in the work-hardening stage gradually increased, indicating the improvement of work-hardening ability. Work-hardening ability can be

measured by work hardening rate θ, which can be calculated by the following Eq. [3]:

$$\theta = \frac{d\sigma_t}{d\varepsilon_t} \qquad [3]$$

σ_t and ε_t are macroscopic true stress and true strain, which can be calculated from engineering stress and engineering strain by Eqs. [4] and [5]:

$$\sigma_t = \sigma(1 + \varepsilon) \qquad [4]$$

$$\varepsilon_t = \ln(1 + \varepsilon) \qquad [5]$$

The true stress–strain and the work hardening curves were plotted to compare the influence of NA and PB on work hardening abilities. As shown in Figures 17(a), (c) and (e), the true stress-strain curves gained from the uniaxial tensile test conducted immediately after solid solution treatment and pre-rolling show a distinct zigzag fluctuation. This phenomenon is caused by the plastic instability of the material, which leads to repeated yield. The plastic instability is called PLC effect, often occurs in some aluminum alloy under certain test temperature and certain strain rate conditions. The PLC effect weakened somewhat after NA, but still existed, and the tensile curve became smoother after PB, indicating that the PLC effect was eliminated. The appearance and disappearance of the PLC effect is related to the state of materials, and is essentially due to the dynamic strain aging phenomenon during the evolution of material microstructure.[33] In the solid solution state, the solute atoms are dispersed in the matrix, during the tensile process, the dislocation is repeatedly pinned and unpinned with solute atoms, resulting in minor fluctuations in the strength of the material. With the extension of NA time, solute atoms aggregation occurs as a precipitated phase. Consequently, the interaction between solute atoms and dislocations gradually diminishes, and the diffusion rate of solute atoms decelerates,
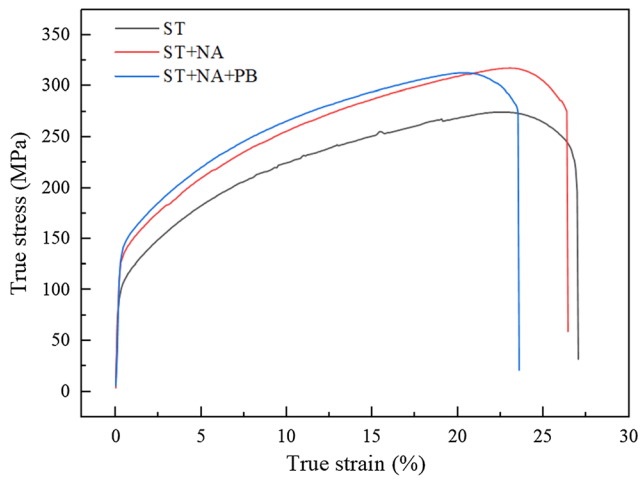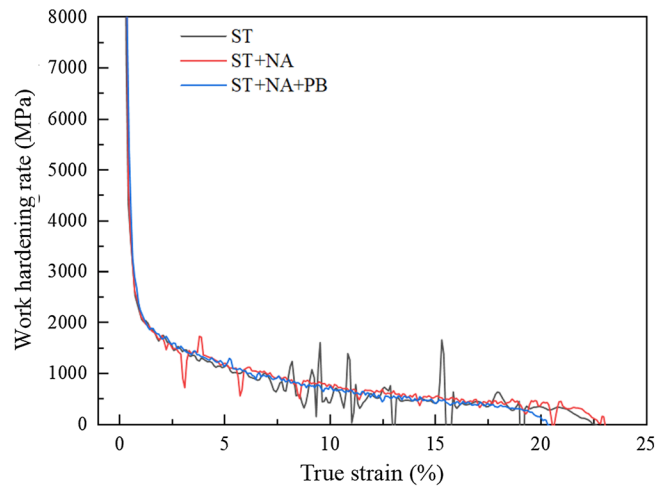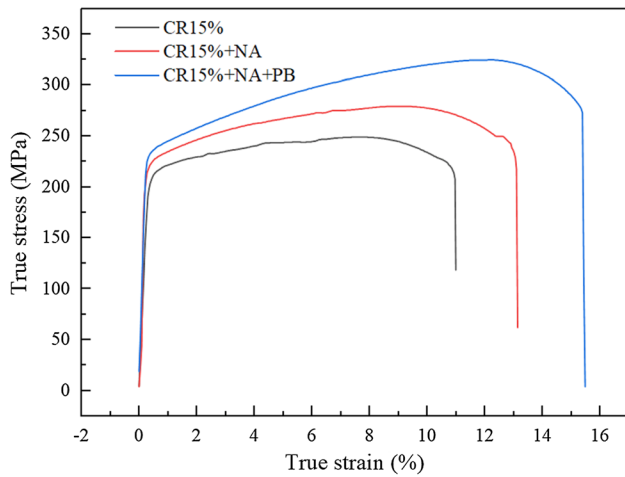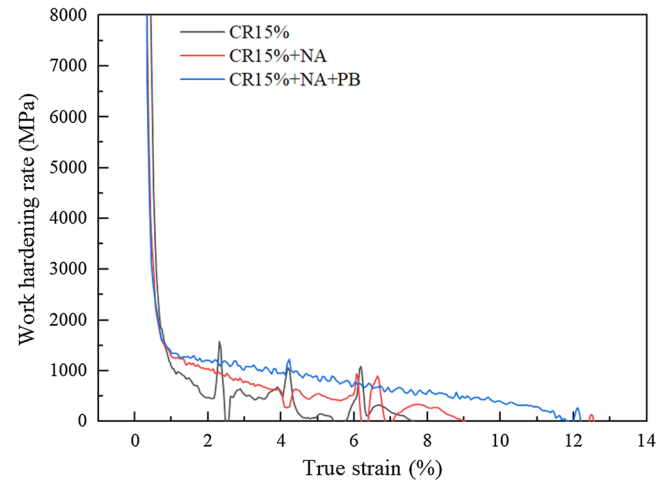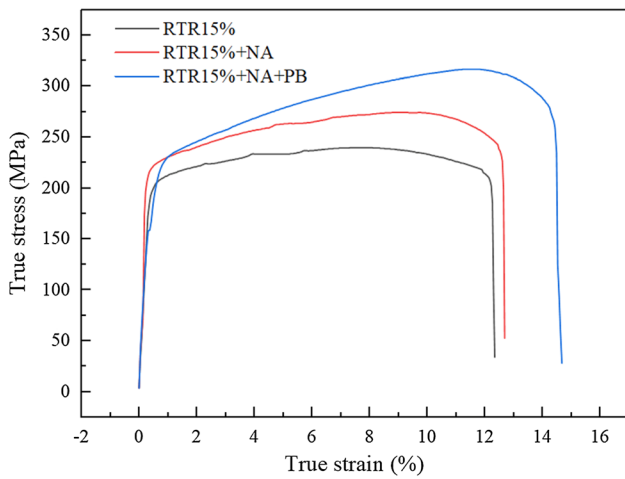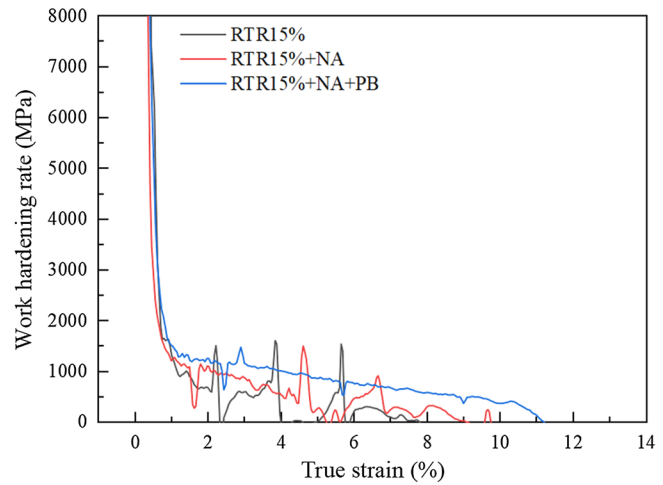
Fig. 17—True stress–strain curves and corresponding work hardening rate curves of (*a*), (*b*) ST, (*c*), (*d*) CR15 pct and (*e*), (*f*) RTR15 pct samples.

ultimately resulting in the attenuation of the PLC. After PB, the microstructure of the alloy tended to be stable and the PLC effect almost disappeared.[34,35]

The work hardening rate curves of each group of samples are shown in Figures 17(b), (d), and (e). It can be seen that there is a sharp downward trend at the beginning stage, which is caused by the transition from
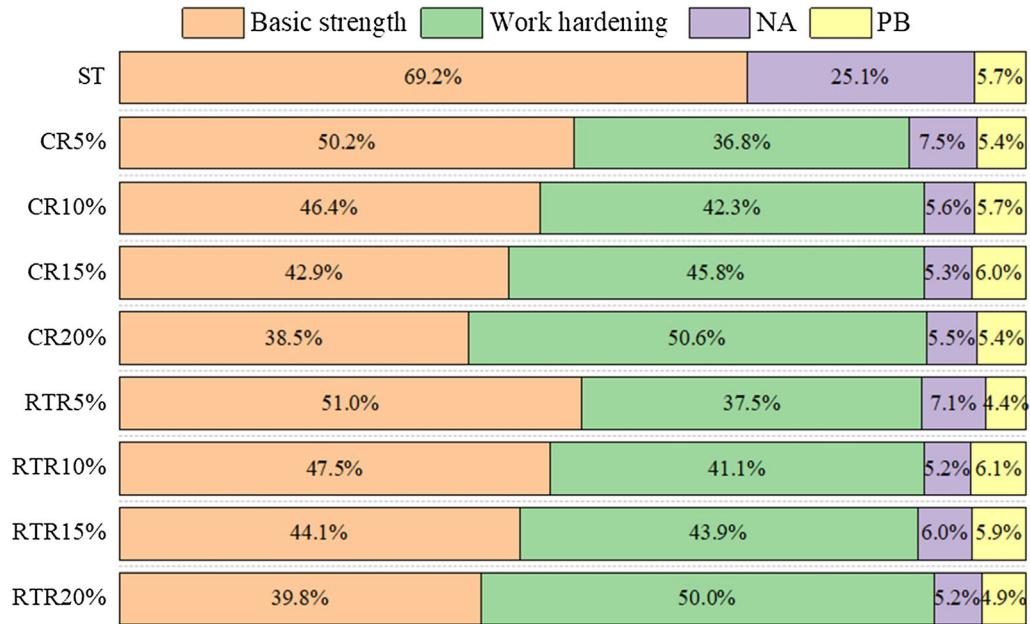
Fig. 18—The YS contribution of each part for the samples after PB.

the elastic stage to the plastic deformation stage. In general, the work hardening rate of samples tends to decrease gradually with an increase in strain level. Due to the PLC effect, the work hardening curves of pre-rolled and pre-rolled + NA samples fluctuate significantly in the declining stage, and the fluctuations decrease a lot after PB. The remaining fluctuations primarily arise from extensometer sliding, sample sliding, and other related factors. The observed trend in work hardening capacity of pre-rolled samples indicated an increase after NA, which further increased after PB. This trend aligns with the corresponding change in UE, as depicted in Figure 13(c). The enhancement of work hardening ability ensures uniformity of plastic deformation during the forming process, as depicted in Figure 17. The synchronization of work hardening and plastic deformation can enhance yield strength and transmission of deformation to non-deformed components, thereby enabling uniform plastic deformation of the metal and ensuring smooth execution of the cold forming process. However, ST sample's work hardening capacity did not change significantly in the NA stage and decreased slightly after PB.

Based on the strength of the material itself, the strength of the samples after PB is affected by three parts: work hardening, NA and PB. The contribution of each part to the final strength is shown in Figure 18. The YS of ST sample without NA is taken as the basic strength, 102.8 ± 0.9 MPa. Since the ST sample was not deformed, the contribution of work hardening to its final strength was zero. At the same time, NA accounted for 25.1 pct of ST sample, the largest among all samples, indicating that NA had the most obvious influence on ST sample. After pre-rolling was introduced, the YS of deformed samples was significantly improved compared with ST sample due to work hardening. The YS

contribution of work hardening for the CR5 pct sample was 36.8 pct. The gradual increase in reduction resulted in a corresponding increase in the work hardening proportion, accounting for 50.6 pct in the CR20 pct sample. The contribution of NA and PB to the final YS were similar, accounting for about 5 pct. In the CR15 pct sample, NA accounts for 5.3 pct, the lowest in the CR samples, and PB contributed 6.0 pct, the highest in the CR samples. Compared with CR samples, the contribution of PB to the final strength of RTR samples was lower, except for the sample with a 10 pct reduction. Combined with the higher forming limit of the CR15 pct sample in the cupping test, it is considered that the pre-cryorolling with reduction of 15 pct is the most appropriate pre-treatment process for the alloy studied in this paper.

In contrast to the obvious increase of YS after pre-rolling, the contribution of work-hardening to UTS for 5 and 10 pct samples was negative, that is, the UTS was reduced. Compared with ST sample, the UTS of CR5 pct, CR10 pct, RTR5 pct and RTR10 pct samples decreased by 8.8, 0.6, 10.4 and 7.3 MPa, respectively. Only when the reduction increased to 15 pct, UTS higher than ST sample again, but the difference was small. This trend persisted even after the NA stage for 2 weeks. This is similar to the study of AA6082 by Qvale et al.[36] and inconsistent with the conventional work hardening phenomenon. It is speculated that the reason for this phenomenon is that the effect of pre-deformation is related to alloy composition, different element contents lead to different precipitation behavior, and different precipitated phases may have different interactions with dislocation. Therefore, the final properties of the alloy may not be affected in the same way. In alloys with high Mg content, the pre-deformation may reduce UTS,[18] which increases the
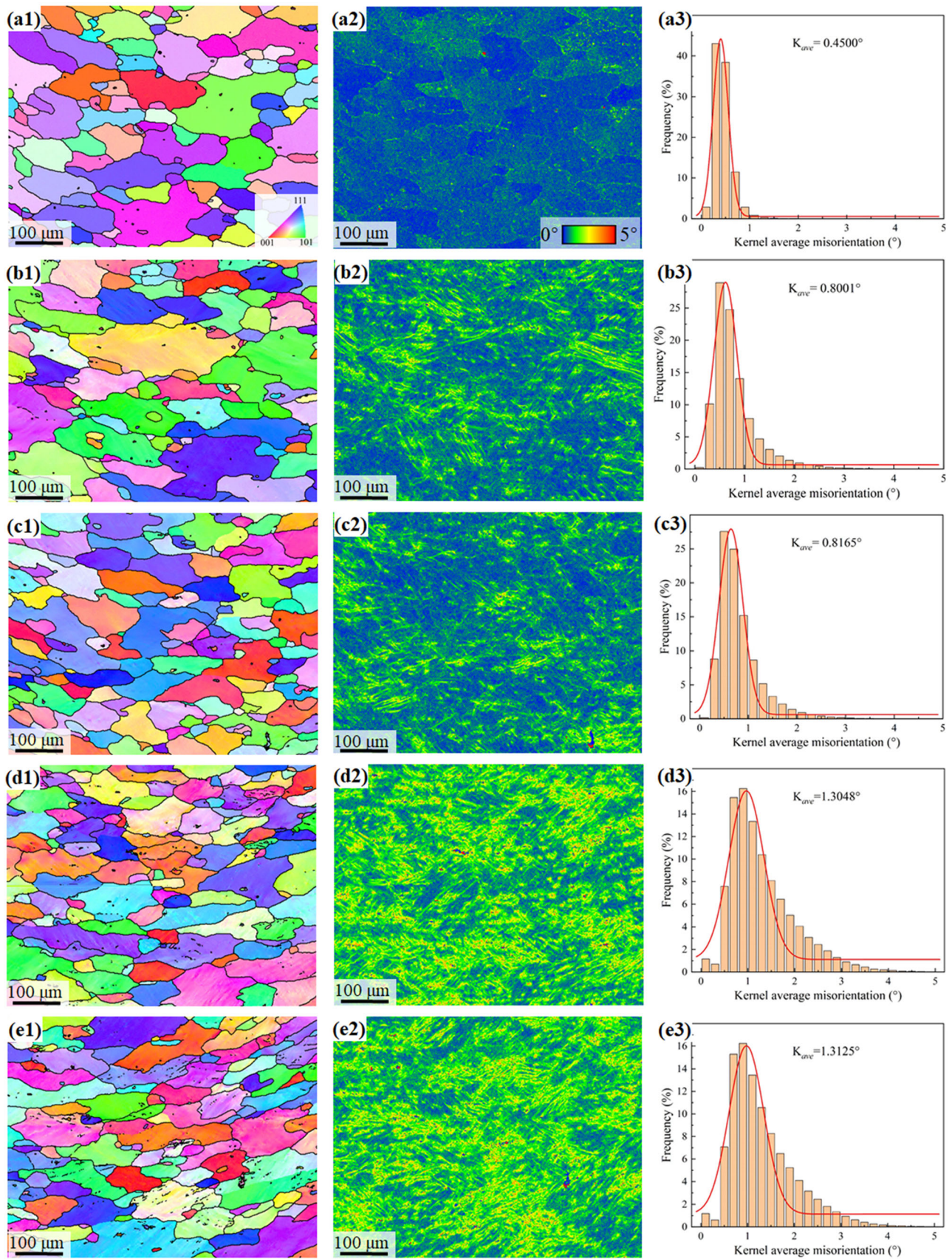
Fig. 19—Microstructures of (*a*) ST, (*b*) RTR5 pct, (*c*) CR5 pct, (*d*) RTR15 pct and (*e*) CR15 pct samples after 2 weeks of NA: (1) IPF maps, (2) KAM maps, and (3) KAM distributions.

difficulty in formulating the pre-deformation process. After PB, the UTS of deformed samples was higher than that of ST sample. Therefore, the main source of UTS improvement was PB, which was more than 10 pct. As the reduction increased, there was a corresponding increase in the (UTS) during the precipitation hardening stage of PB.

B. Relationship Between Microstructure and Mechanical Properties of Samples During NA and PB

According to the mechanical properties results presented in Figures 11 and 12, the hardness and strength of the samples without pre-rolling increased significantly in the NA stage. Specifically, the microhardness and YS increased by 27.2 HV and 37.3 MPa, respectively, which was the most substantial increase observed among all the samples. The consumption of solute atoms by NA led to the formation of numerous clusters (1) in the matrix, resulting in evident negative effects. The Mg/Si ratios of cluster (1) and β'' phase differ significantly. In the PB process, cluster (1) cannot undergo direct transformation into β'' phase or serve as the nucleation site for β'' phase. Instead, they must first dissolve during the heating process, releasing solute atoms, before eventually forming β'' phase.[37,38] As a result, the BHR of ST sample was very low. As shown in Figure 5(d), there was almost no β'' phase in the matrix of ST + NA + PB sample. In terms of mechanical properties, the hardness increased by only 6.5 HV during the PB stage, and YS and UTS increased by 8.5 and 6.2 MPa, respectively, which were the lowest among all the samples. In contrast, the BHR of ST + PB sample (without NA) was 55.4 HV, consistent with the large amount of β'' phase in the Al matrix shown in Figure 5(a).

After the introduction of pre-rolling, a large number of dislocations were generated in the matrix. As shown in Figure 5(e), dislocation entanglement was observed. According to the XRD test calculation, it can be found that the dislocation density in CR15 pct sample was 12 times higher than that in ST sample. Compared with RTR15 pct sample, the dislocation density in CR sample was larger. In addition to the calculation of dislocation density by XRD, we also studied the geometrically necessary dislocation density (ρ_{GND}) on the RD-ND plane of samples by EBSD to further confirm the accuracy of the conclusion. The ρ_{GND} can be estimated by Eq. [6], where θ is the average KAM value (K_{ave}) acquired from KAM distributions, μ is the unit length (1.5 μm for this experiment), and b is Burgers vector, taken as 0.286 nm for Al alloy. As shown in Figure 19, The K_{ave} value of ST sample was 0.45° and it increased significantly due to the room-temperature pre-rolling and pre-cryorolling, indicating a improvement of dislocation density, and the K_{ave} value for CR samples was a bit higher than that of RTR samples. Their ρ_{GND} were $3.66 \times 10^{13}/m^2$ (ST sample), $6.51 \times 10^{13}/m^2$ (RTR5 pct sample), $6.64 \times 10^{13}/m^2$ (CR 5 pct sample), $1.062 \times 10^{14}/m^2$ (RTR 15 pct sample) and $1.068 \times 10^{14}/m^2$ (CR 15 pct sample), respectively. This result was consistent with the XRD test calculation.

$$\rho_{GND} = \frac{2\theta}{\mu b} \qquad [6]$$

Dislocation can act as the sinks of vacancies and inhibit spontaneous clustering at room temperature, thus reducing the negative effect of NA.[39] Compared with ST sample, the hardness increment of pre-rolled samples in NA stage was reduced by 41.5 to 50 pct, while increment of YS and UTS decreased by 58.7 to 69.7 and 5 to 29 pct, respectively. The pre-rolled samples exhibited a reduced influence of NA, the precipitation of cluster (1) was inhibited in them, which could also be verified by the DSC curve shown in Figure 20. All curves had an obvious exothermic peak near 523 K, which was denoted as peak 1. The other exothermic peak near 573 K was denoted as peak 2. According to the precipitation sequence of Al–Mg–Si alloy and previous studies, it is believed that peak 1 and peak 2 correspond to β'' phase and β' phase, respectively.[40,41] The endothermic peak observed in the ST sample between 473 and 498 K can be attributed to the dissolution of clusters. However, this peak was notably absent or weakened in the DSC curves of the other four samples. This suggests pre-rolled samples did not undergo cluster dissolution during the heating process, indicating that pre-rolling can effectively inhibit cluster formation during the NA process.[19] As a result, the solute atoms were retained, making it easier to form the β'' phase. Compared with ST sample, peak 1 of pre-rolled samples moved to low temperature area and its intensity became lower, ST (527.6 K), RTR10 pct (520.6 K), CR10 pct (517.4 K), RTR20 pct (514.2 K), and CR20 pct (509.7 K), which mean that pre-rolling promoted β'' phase's precipitation and the promotion effect was more obvious in CR samples with large reduction. For CR samples, the increment of YS and UTS during PB increased 30.6 to 70.6 pct and 341.9 to 580.6 pct, respectively, compared with ST sample when the reduction increased from 5 to 20 pct. In addition, it was observed that the exothermic peak corresponding to peak 2 in pre-rolled samples exhibited a rightward shift towards higher temperature
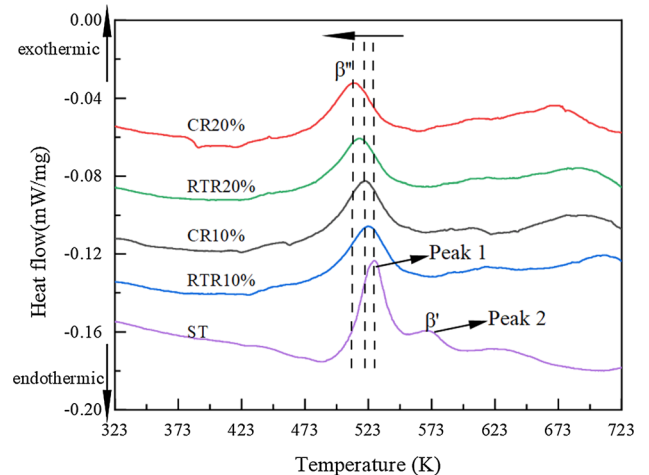

Fig. 20—DSC curves of samples deformed under different reductions after 2 weeks of NA.
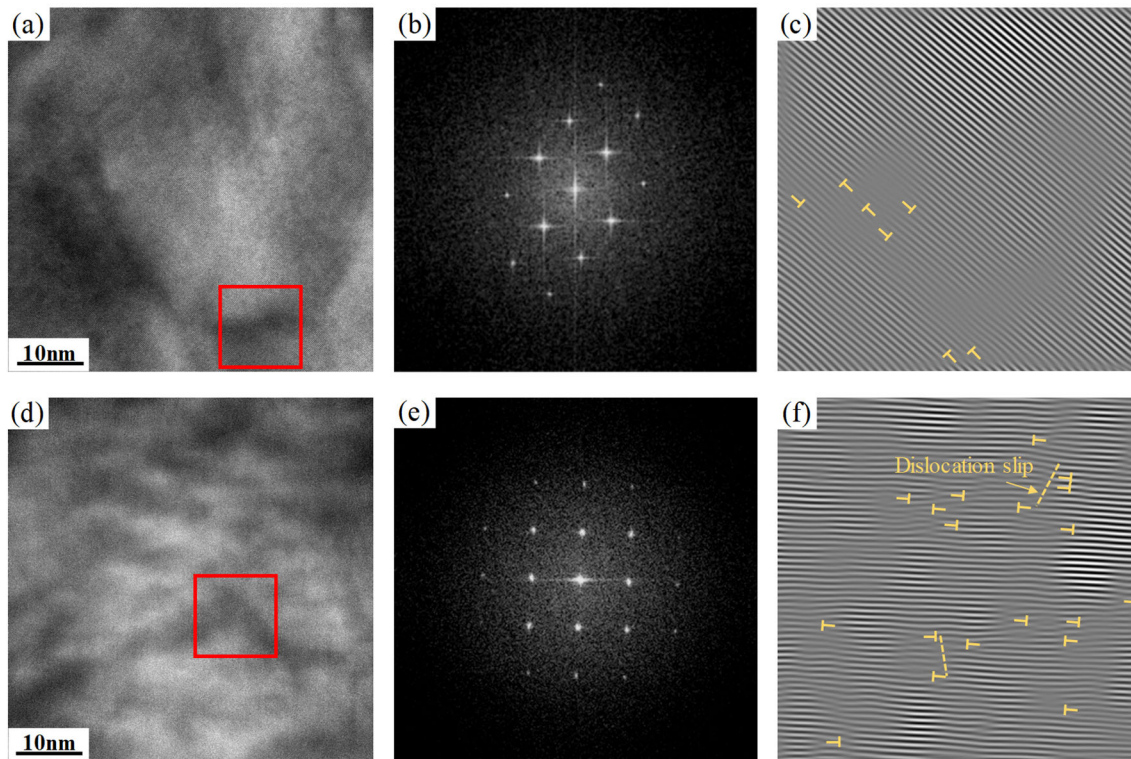
Fig. 21—HRTEM images of the (*a*) RTR15 pct sample, (*b*) FFT and (*c*) IFFT of the red rectangular region in (a), (*d*) CR15 pct sample, (*e*) FFT and (*f*) IFFT of the red rectangular region in (d), with dislocation marked by '⊥' symbols (Color figure online).

area. This shift suggests that the formation of the *β'* phase was impeded due to pre-rolling and pre-rolled samples are less likely to occur overaging during the heating process.

When the sample deforms at cryogenic temperature, the dynamic recovery is inhibited, which can further refine the grains and accumulate high density dislocation compared with room temperature deformation.[21–24] As seen from the optical micrographs (Figures 3 and 4) and XRD calculation result (Table III), with the same reduction, the average grain size of CR samples was smaller than that of RTR samples, and its dislocation density was higher. The advantages of cryogenic deformation brought about two distinct effects. Firstly, the smaller grain size led to higher original strength, as evidenced by the outcomes of uniaxial tensile tests (Figure 12(a)). Secondly, higher dislocation density resulted in bigger BHR, as shown in Figure 13.

In order to observe the dislocation distribution in pre-rolled samples at different temperatures, Inverse Fast Fourier transform (IFFT) was performed on the high-resolution TEM images of CR15 pct sample and RTR15 pct sample. According to the IFFT images shown in Figures 21(c) and (f), the microstructure and dislocation accumulation of the two samples differed greatly. The dislocation density of CR15 pct sample was higher than that of RTR15 pct sample, consistent with the XRD results in Table II, and showing obvious slip characteristics. However, the number of dislocations in RTR15 pct sample was small and distributed dispersively.
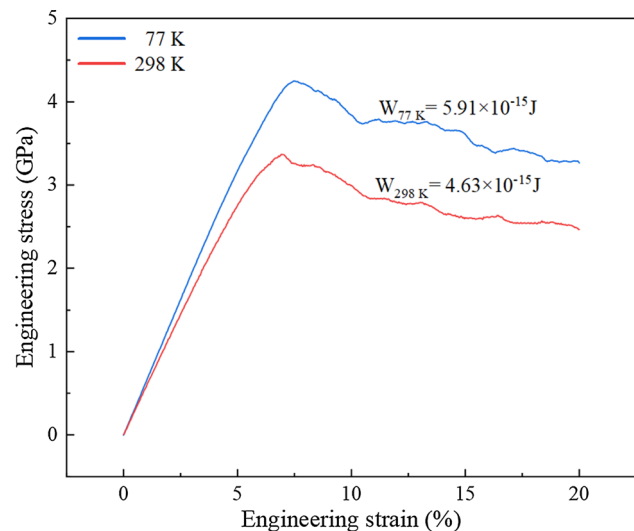

Fig. 22—Engineering stress–strain curves of Al–0.92Mg–0.48Si system deformed at 77 K and 298 K.

In addition to analyzing the dislocation density through microscopic characterization, we also quantitatively analyzed the differences in dislocation density and types between samples deformed at cryogenic and room temperatures by molecular dynamics simulation. As depicted in Figure 10, the perfect dislocation density of the model deformed at 77 K was close to that at 298 K, while the Shockley partial dislocation density was higher, resulting in a higher dislocation density at 77 K

during the initial stages of deformation ($\varepsilon < 5$ pct). With the increase of engineering strain, the perfect dislocation density gradually decreased while the Shockley partial dislocation density increased, and the growth rate was faster at 298 K than 77 K. When the engineering strain was between 5 and 6 pct, the content of Shockley partial dislocation increased rapidly at 298 K, causing the total dislocation density to approach and even exceed that at 77 K. In the model deformed at 77 K, the Shockley partial dislocation began to increase significantly after the engineering strain was 6 pct, and then the dislocation density in the two models was close. When the engineering strain was 10 pct, the maximum value of total dislocation density appeared and their values were 2.02×10^{17} m^{-2} (77 K) and 1.95×10^{17} m^{-2} (298 K), respectively. After that, the total dislocation density began to decline, and the Shockley partial dislocation density decreased faster in the model deformed at 298 K, resulting in the total dislocation density quickly lower than that at 77 K. However, their perfect dislocation density was very close and stable, which was 0.2×10^{17} m^{-2}, and this trend maintained until the end of deformation. According to the density variation trend of Shockley partial dislocation and total dislocation at two temperatures, the response of dislocation in the model deformed at 77 K was slower than that at 298 K. This phenomenon was related to increased strain energy and critical nucleation stress of dislocation at a cryogenic temperature,[42] so the strain energy in both deform processes was calculated. Figure 22 shows the engineering stress-strain curves during simulative compression deformation. The stress peak occurred near $\varepsilon = 9$ pct, and then gradually decreased. Under the same deformation amount, the stress at 77 K was larger than that at 298 K, indicating greater deformation resistance and strain energy in cryogenic deformation. Strain energy (W) can be calculated by the equation: $W = V \times S(\varepsilon)$, where V is the initial volume of the model, and $S(\varepsilon)$ is the area under the engineering stress-strain curve. The stress energy of the model deformed at 77 K was 5.91×10^{-15} J, 27.6 pct higher than that at 298 K (4.63×10^{-15} J).

Based on prior research, Al–Mg–Si alloys with a high Mg/Si ratio are significantly impacted by the adverse effects of NA. During the NA phase, the properties and microstructure of the alloys undergo noticeable alterations, leading to a reduced proportion of PB to the final properties, as shown in Figure 11. In prospective research endeavors, Al–Mg–Si alloys with a small or medium Mg/Si ratio, may be utilized for investigation. The present study introduces a novel approach to enhance the pre-treatment process by incorporating cryogenic treatment into the conventional pre-deformation process, thereby augmenting the BHR. This is a simple and adaptable method, which has a broad application prospect.

V. CONCLUSIONS

1. During paint baking, the effect of pre-cryorolling on bake hardening response was more obvious than that of room-temperature pre-rolling. Specifically, the hardness, yield strength and ultimate tensile strength of ST sample increased by 6.5 HV, 8.5 and 6.2 MPa, respectively. RTR20 pct sample increased by 13.7 HV, 12.8 and 33.9 MPa, respectively. While for CR20 pct sample, the increments were 16.3HV, 14.5 and 42.2 MPa, respectively. In addition, the total elongation of CR samples after paint baking was higher than that of RTR samples. Considering the formability and bake hardening response, pre-cryorolling with a reduction of 15 pct is considered to be the most appropriate pre-treatment method for the alloy studied in this paper.

2. The dislocation introduced by pre-rolling inhibited the formation of clusters in natural aging process, and provided nucleation sites for precipitates, thus improving the bake hardening response. Through XRD calculation, EBSD and HRTEM, it can be found that under the same reduction, the dislocation density introduced by pre-cryorolling was higher than room temperature pre-rolling, leading to a larger bake hardening response.

3. During the compression process of Al–0.92Mg–0.48Si system at nm scale, dislocation rings were preferentially formed near solute atoms in the grain due to lattice distortion, and the perfect dislocations at the grain boundary gradually split into Shockley partial dislocations. The low temperature inhibited the movement of dislocation and slowed its annihilation rate from slip out of the surface of the system. As a result, the change of dislocation in the model deformed at 77 K was delayed compared with that at 298 K, and higher dislocation density was eventually accumulated.

CONFLICT OF INTEREST

The authors declare that they have no known competing financial interests or personal relationships that could have appeared to influence the work reported in this article.

REFERENCES

1. S.N. Khangholi, M. Javidani, A. Maltais, and X.G. Chen: *J. Mater. Res.*, 2022, vol. 37, pp. 670–91.
2. G. Gao, X. Li, L. Yan, B. Xiong, Z. Li, Y. Zhang, K. Wen, and Y. Li: *J. Cent. South Univ.*, 2022, vol. 29, pp. 950–59.
3. J. Hirsch and T. Al-Samman: *Acta Mater.*, 2013, vol. 61, pp. 818–43.
4. G.A. Edwards, K. Stiller, G.L. Dunlop, and M.J. Couper: *Acta Mater.*, 1998, vol. 46, pp. 3893–3904.
5. Y. Aruga, M. Kozuka, Y. Takaki, and T. Sato: *Metall. Mater. Trans. A*, 2014, vol. 45A, pp. 5906–13.
6. E. Hodžić, J. Domitner, A. Thum, A.S. Sabet, N. Müllner, W. Fragner, and C. Sommitsch: *J. Manuf. Process.*, 2023, vol. 94, pp. 228–39.
7. Z. Yang, X. Jiang, X. Zhang, M. Liu, Z. Liang, D. Leyvraz, and J. Banhart: *Scripta Mater.*, 2021, vol. 190, pp. 179–82.
8. S. Jin, T. Ngai, L. Li, Y. Lai, Z. Chen, and A. Wang: *J. Alloys Compd.*, 2018, vol. 742, pp. 852–59.
9. F. Badkoobeh, A. Nouri, and H. Hassannejad: *Mater. Sci. Eng. A*, 2020, vol. 770, p. 138544.
10. K. Chen, C. Liu, P. Ma, J. Yang, L. Zhan, M. Huang, and J. Hu: *Mater. Sci. Eng. A*, 2021, vol. 826, p. 141967.
11. L. Zhu, M. Guo, Y. Wu, H. Zhu, and J. Zhang: *J. Mater. Res. Technol.*, 2022, vol. 18, pp. 1009–16.
12. S. Duan, F. Guo, D. Wu, T. Wang, T. Tsuchiya, K. Matsuda, and Y. Zou: *J. Mater. Res. Technol.*, 2021, vol. 15, pp. 2379–92.
13. X. Chen, D. Kim, O. Minho, C.D. Marioara, S.J. Andersen, A. Lervik, R. Holmestad, and E. Kobayashi: *Mater. Sci. Eng. A*, 2021, vol. 820, p. 141557.
14. M. Elsayed, T.E.M. Staab, J. Čížek, and R. Krause-Rehberg: *Acta Mater.*, 2021, vol. 219, p. 117228.
15. H. Li and W. Liu: *Metall. Mater. Trans. A*, 2017, vol. 48A, pp. 1990–98.
16. D. Yin, Q. Xiao, Y. Chen, H. Liu, D. Yi, B. Wang, and S. Pan: *Mater. Des.*, 2016, vol. 95, pp. 329–39.
17. Z. Jia, L. Ding, Y. Weng, Z. Wen, and Q. Liu: *Trans. Nonferr. Met. Soc. China*, 2016, vol. 26, pp. 924–29.
18. Z. Yuan, C. Lu, L. Ding, K. Xiang, Y. Weng, Q. Liu, and Z. Jia: *Mater. Sci. Eng. A*, 2022, vol. 849, p. 143495.
19. A. Serizawa, T. Sato, and M.K. Miller: *Mater. Sci. Eng. A*, 2013, vol. 561, pp. 492–97.
20. S. Zhu, H. Shih, X. Cui, C. Yu, and S.P. Ringer: *Acta Mater.*, 2021, vol. 203, p. 116455.
21. H. Xiong, L. Su, C. Kong, and H. Yu: *Adv. Eng. Mater.*, 2021, vol. 23, p. 2001533.
22. L. Li, H. Kang, S. Zhang, R. Li, X. Yang, Z. Chen, E. Guo, and T. Wang: *J. Alloys Compd.*, 2023, vol. 938, p. 168656.
23. F. Yu, Y. Zhang, C. Kong, and H. Yu: *Mater. Sci. Eng. A*, 2022, vol. 834, p. 142600.
24. J. Liu, Y. Wu, H. Gao, C. Kong, and H. Yu: *Metall. Mater. Trans. A*, 2023, vol. 54A, pp. 16–22.
25. M. Cui, Y.H. Jo, S.H. Kayani, H. Kim, and J. Lee: *J. Mater. Res. Technol.*, 2022, vol. 20, pp. 2629–37.
26. B. Jelinek, S. Groh, M.F. Horstemeyer, J. Houze, S.G. Kim, G.J. Wagner, A. Moitra, and M.I. Baskes: *Phys. Rev. B*, 2012, vol. 85, p. 245102.
27. P. Hirel: *Comput. Phys. Commun.*, 2015, vol. 197, pp. 212–19.
28. A. Stukowski: *Modell. Simul. Mater. Sci. Eng.*, 2010, vol. 18, p. 015012.
29. P.H. Ninive, A. Strandlie, S. Gulbrandsen-Dahl, W. Lefebvre, C.D. Marioara, S.J. Andersen, J. Friis, R. Holmestad, and O.M. Løvvik: *Acta Mater.*, 2014, vol. 69, pp. 126–34.
30. C.D. Marioara, S.J. Andersen, J. Jansen, and H.W. Zandbergen: *Acta Mater.*, 2001, vol. 49, pp. 321–28.
31. S. Pal, P.N. Babu, B.S.K. Gargeya, and C.S. Becquart: *Mater. Chem. Phys.*, 2020, vol. 243, p. 122593.
32. H. Li, P. Chen, Z. Wang, F. Zhu, R. Song, and Z. Zheng: *Mater. Sci. Eng. A*, 2019, vol. 742, pp. 798–812.
33. H. Zhong, P.A. Rometsch, Q. Zhu, L. Cao, and Y. Estrin: *Mater. Sci. Eng. A*, 2017, vol. 687, pp. 323–31.
34. T. Mäkinen, P. Karppinen, M. Ovaska, L. Laurson, and M.J. Alava: *Sci. Adv.*, 2020, vol. 6, p. eabc7350.
35. C.H. Wu, H. Li, T.J. Bian, C. Lei, and L.W. Zhang: *Mater. Charact.*, 2022, vol. 184, p. 111694.
36. K. Qvale, O.S. Hopperstad, O. Reiso, U.H. Tundal, C.D. Marioara, and T. Børvik: *Thin Wall Struct.*, 2021, vol. 158, p. 107160.
37. V. Fallah, B. Langelier, N. Ofori-Opoku, B. Raeisinia, N. Provatas, and S. Esmaeili: *Acta Mater.*, 2016, vol. 103, pp. 290–300.
38. M. Song, E. Kobayashi, and J. Kim: *J. Alloys Compd.*, 2023, vol. 946, p. 169291.
39. K. Wu, G. Liu, P. Yu, C. Ye, J. Shi, and Y. Shen: *Int. J. Plast.*, 2022, vol. 149, p. 103160.
40. G. Li, M. Guo, J. Du, and L. Zhuang: *Mater. Des.*, 2022, vol. 218, p. 110714.
41. L. Zhu, M. Guo, and J. Zhang: *Mater. Sci. Eng. A*, 2022, vol. 841, p. 143016.
42. S. Dai, Z. Xie, and Y. Wang: *Int. J. Plast.*, 2022, vol. 149, p. 103155.